Towards geometrical calibration of X-ray computed tomography systems – A review

Massimiliano Ferrucci[1,2], Richard K Leach[1,*], Claudiu Giusca[1], Wim Dewulf[2], Simone Carmignato[3]

[1] National Physical Laboratory, Teddington, TW11 0LW United Kingdom
[2] Mechanical Engineering Department, KU Leuven, Belgium
[3] Università degli studi di Padova, Padova, Italy
[*] New correspondence: Department of Mechanical, Materials and Manufacturing Engineering, University of Nottingham, Nottingham, NG7 2RD United Kingdom

Abstract

Industrial X-ray computed tomography (XCT) is seen as a potentially effective tool for industrial inspection of complex parts. In particular, XCT is an attractive solution for the measurement of internal geometries, which are inaccessible by conventional coordinate measuring systems (CMSs). While the technology is available and the benefits are recognized, methods to establish measurement assurance of XCT systems are lacking. More specifically, assessment of measurement uncertainty and the subsequent establishment of measurement traceability is a largely unknown process. This paper is a review of research that contributes to the development of a geometrical calibration procedure for XCT systems. A brief introduction to the geometry of cone-beam tomography systems is given, after which the geometrical influence factors are outlined. Mathematical measurement models play a significant role in understanding how geometrical offsets and misalignments contribute to error in measurements; therefore, the application of mathematical models in simulating geometrical errors is discussed and the corresponding literature is presented. Then, the various methods that have been developed to measure certain geometrical errors are reviewed. The findings from this review are discussed and suggestions are provided for future work towards the development of a comprehensive and practical geometrical calibration procedure.

1   INTRODUCTION

X-Ray computed tomography (XCT) is an imaging technique that employs the attenuating properties of a medium as X-rays propagate through it. Since the early days of its commercialization, XCT has been widely used in the medical field as a method to image inside the human body [1]. The technology was later adapted for industrial inspection of manufactured parts. Particularly valuable to manufacturers is the ability to inspect the material structure of their manufactured product in a manner that would not compromise the product's physical integrity. More recently, XCT has been recognized as an effective tool for coordinate measurement of assembled and complex parts [2]. In particular, XCT provides the user with the ability to perform dimensional analysis on internal features that are inaccessible by conventional coordinate measuring systems (CMSs) [3].

In the interest of conciseness, the principles of X-ray computed tomography are discussed briefly. References [4,5] provide an extensive overview of the principles of XCT. The XCT process begins with the generation of the X-ray radiation. An X-ray tube consists of a cathode filament on one end and an anode on the opposite end. When the cathode filament is heated, electrons are released from the surface of the filament. A difference in electric potential between the cathode and the anode accelerates these

'free' electrons in the direction of the anode. As the accelerated electrons reach the anode, they are focused onto a target, resulting in the emission of X-ray photons. These photons are then directed towards the work piece. As the X-rays travel through the work piece, their intensity is attenuated. Attenuation occurs as a result of the interaction of the X-rays and the work piece material, namely photoelectric absorption and scattering [1]. The amount of attenuation through a specific material depends on the energy (wavelength) of the X-ray radiation and several characteristics of the material, such as its density, its element number, and the length of penetration of the X-rays through the material. X-rays that are not completely attenuated by the object are transmitted to a detector. The intensity of the incident X-rays is registered by the detector and is converted to a digital signal. Each pixel registers the intensity of the X-rays after having traversed the linear trajectory from the source to the respective pixel position on the detector. The collection of pixel intensities is stored as a radiographic image (also known as a radiograph). The total attenuation of the X-rays along a given path can be determined from the registered intensity values and the intensity of the non-attenuated X-rays. A radiograph, therefore, ideally represents the distribution of attenuated X-rays along the traversed volume. Radiographs are taken at multiple object viewing angles.

A three-dimensional volumetric model of the work piece can be generated by way of tomographic reconstruction on the set of radiographs. Just as an image is comprised of pixels, the volumetric model consists of three-dimensional voxels (volumetric pixels). Each voxel is characterized by a grey value corresponding to the local material attenuation at the voxel position within the measurement volume [6]. The grey value of the voxels can be used to extract surface information from the volumetric model. Since the grey values correspond to varying material properties, the edge between two materials can be defined by a transition in grey values. A surface model can be generated by detecting edges between features with different material attenuation by way of grey value thresholds. Subsequently, surface points can be extracted by defining a sampling interval on the surface model. The resulting surface points can then be used for dimensional analysis of the work piece.

As XCT is adopted by manufacturers and other industrial users, there is a strong demand for performance standards and calibration procedures. In particular, the assessment of measurement uncertainty is critical to the application of XCT for traceable coordinate metrology [7,8]. The uncertainty of coordinate measurements made on an XCT system is a result of various influence factors in the measurement procedure [9]. Geometrical offsets, misalignments, and instabilities can result in scaling and reconstruction errors, both of which are detrimental to the quality of coordinate measurements made on industrial XCT systems. For this reason, it is important that users are provided with a procedure they can use to evaluate the geometry of their XCT system. It should be noted that geometrical calibration alone is not enough to allow a user to determine measurement uncertainty as non-geometrical influence factors exist. However, geometrical calibration is a critical step towards assessing XCT measurement uncertainty and achieving measurement traceability.

This paper is a review of the current research on the development of methods to determine geometrical influence factors in XCT systems and to understand their effects on measurement uncertainty. In section 2, the ideal geometrical construction of industrial XCT systems is presented. Subsequently, the geometrical influence factors are identified in section 3. Section 4 is dedicated to the application of mathematical models in evaluating the sensitivity of measurements to geometrical errors. In section 5, the methods that have been developed to determine geometrical influence factors are described. The findings of the review are summarized in section 6 along with a discussion on research opportunities for geometrical calibration of industrial XCT systems.

2

2   INSTRUMENT GEOMETRY

The construction of an XCT system is based on the concepts of projective geometry. X-rays are projected from a source onto a detector; the shape of the detector depends on the shape of the X-ray beam. Industrial XCT systems employ one of two X-ray beam shapes. The first is a cone-shaped beam, which is characterized by a spherical wave-front that diverges as it propagates away from the source. The detector in a cone-beam system is a flat two-dimensional panel. The second type of X-ray beam is fan-shaped (fan-beam), which is incident on either a straight or curved line detector. In order for a fan-beam system to image the same area as a cone-beam system, multiple linear slices must be taken and stitched together [10]. Some of the benefits of fan-beam systems include reduction in the scattered radiation that is measured by the smaller detector, as well as elimination of cone-beam effects due to the parallel beam geometry. A detailed discussion of the benefits and shortfalls of each beam shape is found elsewhere [1,6]. Recent publications suggest that cone-beam XCT systems are more prevalent in research laboratories [11,12]. For most measurement tasks, the larger area of the flat panel detector in cone-beam systems provides an increased rate of data collection when compared to the line detectors in fan-beam systems. Thus, the focus of this paper is mostly on typical cone-beam XCT systems.

The geometry of industrial cone-beam XCT systems is defined by the relative position and orientation of the three major components: the X-ray source, the rotation stage, and the detector. Global coordinate axes are defined for the purpose of describing the ideal system geometry (figure 1). The magnification axis, also the Z axis, is given by the linear path from the centre of the X-ray source to the detector. The Y axis is parallel to the rotation axis. The X axis is orthogonal to both the Y and Z axes, thus forming a Cartesian coordinate system. It should be noted that the coordinate system defined here may be different from the coordinate systems used in some of the referenced literature. In many industrial XCT systems, the rotation axis can be translated along three directions; ideally, these directions are parallel to the X, Y, and Z axes of the global coordinate frame. Translations along X and Y are used to position the work piece into and out of the field of view, whereas translation along Z controls the magnification of the object's projection onto the detector.
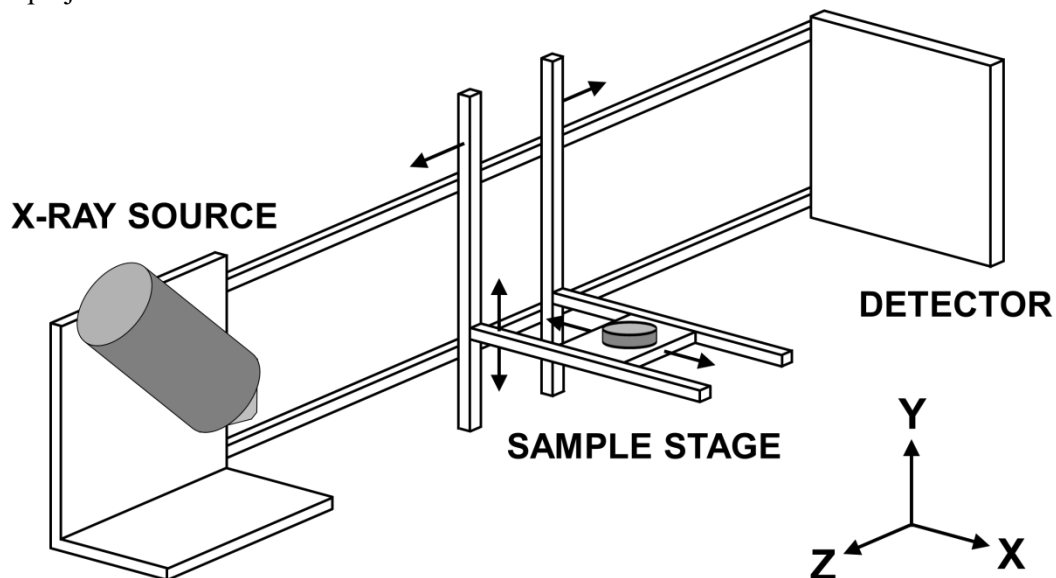

Figure 1. The linear path from the X-ray source to the detector defines the magnification axis. The Y axis is parallel to the rotation axis. The X axis is orthogonal to both the Y and Z axes, forming a Cartesian coordinate system. A flat panel detector, which corresponds to cone-beam XCT systems, is shown. This diagram shows one type of construction of XCT systems; however, other architectures are possible.

3   GEOMETRICAL INFLUENCE FACTORS

For a fixed position of the rotation stage, a cone-beam XCT system is considered aligned when it satisfies the following conditions (figure 2):

(i)   the intersection of the magnification axis with the detector (also known as the principal point – a term used in geometrical modelling of cameras [13]) is coincident with the centre of the detector,

(ii)   the magnification axis is normal to the detector,

(iii)   the magnification axis intersects the axis of rotation at a 90° angle1, and

(iv)   the projection of the axis of rotation is parallel to the detector's columns.

Any deviations from these ideal conditions are considered influence factors and can contribute to errors in dimensional measurements.
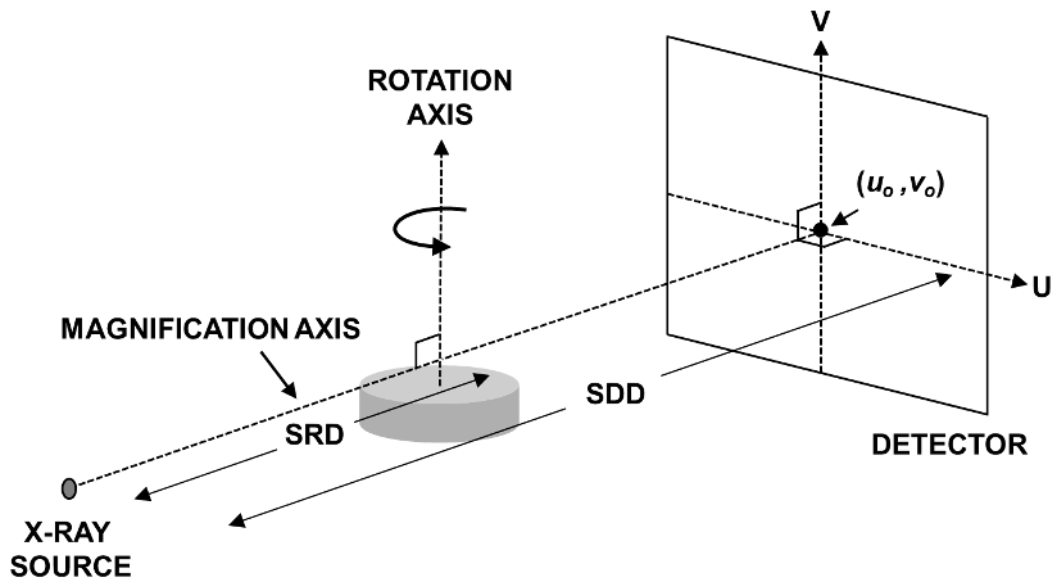

Figure 2. An aligned cone-beam XCT system satisfies a series of conditions shown in this diagram. Any deviation from these ideal conditions is considered a geometrical influence factor.

Deviations from ideal alignment are parameterized in the literature. For example, deviations from condition (i) can be described by the pixel position (u_o, v_o) of the principal point. Deviations from condition (ii) are described by two out-of-plane rotations θ and φ of the detector (figure 3a,b). If the magnification axis does not intersect the rotation axis (condition (iii)), the rotation axis is said to have an X offset m. The parameter m is used in the literature and corresponds to a 'mechanical offset' of the rotation axis, not to be mistaken with the magnification factor M. Generally, a Y offset of the rotation axis is only of consequence for scans that require translation of the stage along Y (fan-beam CT). Also, if the rotation axis is not orthogonal to the magnification axis, the rotation axis is said to have a tilt θ_r (figure 3c). A deviation from condition (iv) is an in-plane rotation of the detector η (figure 3d). Additionally, the distance from X-ray source to rotation axis, *SRD,* and the distance from X-ray source

---

1 It should be noted that the 90° angle of intersection in condition (iii) is only applicable to systems that do not allow intentional tilts of the rotation axis. Also, in some cases the magnification axis and rotation axis are separated by an intentional shift along X. Such a shift is acceptable if the reconstruction algorithm is adapted accordingly.

to detector, *SDD*, are assumed to be accurately known. Any discrepancy between assumed distance and actual distance will result in a global scaling error. The angular index α of the rotation axis is also assumed known; an error in the angular index results in reconstruction errors. Also, the detector plane is assumed to be perfectly planar and the pixels uniform. Deviations in this respect are considered planar distortions of the detector. Detector distortions cannot be described by one parameter; instead, they are often described by a polynomial function. The parameters that describe the geometry of an XCT system for a fixed rotation stage position are shown in
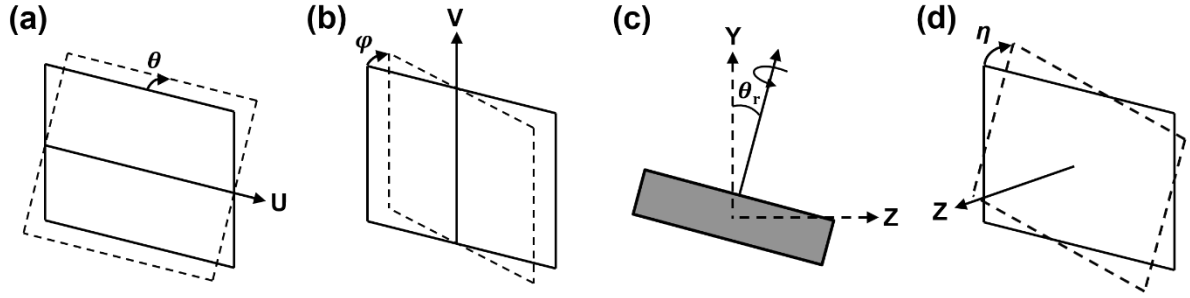
table 1.

Figure 3. Some of the geometrical influence factors in cone-beam XCT systems include (a) detector tilt θ, (b) detector slant φ, rotation axis tilt θ_r, and (d) detector in-plane rotation η.

Table 1. The geometry of a cone-beam XCT system for a fixed kinematic position of the rotation stage can be described by the set of parameters shown here.

Parameter	Description
SRD	Source-to-rotation axis distance
SDD	Source-to-detector distance
u_o	Detector offset (X)
v_o	Detector offset (Y)
θ	Detector tilt (out-of-plane)
φ	Detector slant (out-of-plane)
η	Detector skew (in-plane)
m	Rotation axis offset (X)
θ_r	Rotation axis tilt (about X)
α	Angular index of rotation axis
No variable	Planar distortions of the detector

In addition to deviations of each component from the ideal geometry, error motions can occur in the translation and rotation of the stage. Rotation stage translation is achieved by way of precision guideways; linear encoders or other distance sensors monitor the position of the rotation stage on each kinematic axis separately. Offsets between linear indexed position and actual position are considered positioning errors. Ideally, the Z axis is parallel to the magnification axis while the other two axes should be orthogonal to the Z axis and mutually orthogonal. A deviation from these conditions is considered a squareness error of the kinematic axes. Straightness errors can also exist and are defined as transverse deviations of each axis from straight line movement [14]. Errors in the mechanical motion of the kinematic axes directly affect the parameters describing the position and orientation of the rotation axis. For example, positioning errors of the Z axis as well as squareness and straightness errors of the X and Y axes along the Z direction will result in an error in *SRD*. Alternatively, positioning errors of the X

axis as well as squareness and straightness errors of the Y and Z axes along the X direction will result in an error of m. Errors along the Y direction are only considered if translation of the rotation stage along the Y axis is required, such as for fan-beam systems. Kinematic axes can also exhibit rotational behaviours (roll, pitch, and yaw) as a function of axis position, which translate to tilts of the rotation stage with respect to the fixed gantry (θ_r and η).

Typically, a reconstruction algorithm is based on the assumption that the position and orientation of the rotation axis does not deviate during the scan (except, of course, for its intended rotation). However, rotary axes are shown to exhibit error motions as a function of rotation position (figure 4), resulting in both scaling and reconstruction errors. The measurement of kinematic error motions has been studied rigorously for contact-probe CMMs (see, for example, references [15–26]). Drift of the X-ray source is a known phenomenon in XCT systems [1,27]. A drift of the X-ray source along the Z axis will result in a drift of both SDD and SRD, whereas drift along X and Y will cause a lateral drift in the projected image.
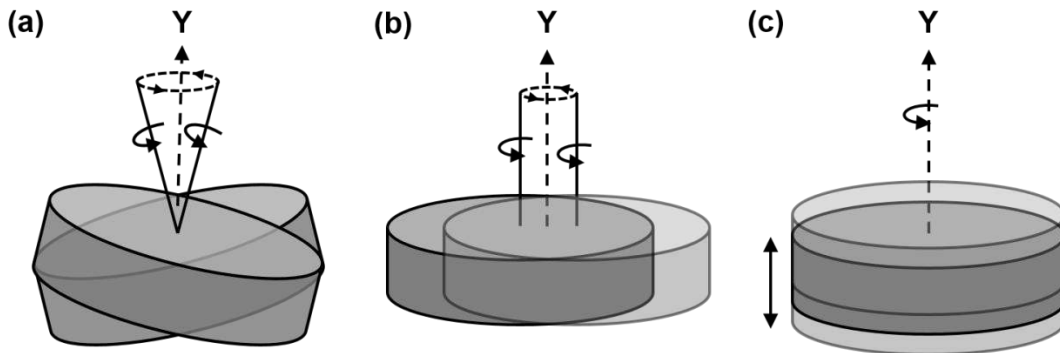

Figure 4. Instabilities of the rotary axis, such as (a) tilt error motion, (b) radial error motion, and (c) axial error motion, can result in scaling and reconstruction errors.

4   MEASUREMENT MODEL

A useful step in trying to understand the performance of a measurement system is by way of a measurement model. The behaviour of a particular system can be described by mathematical expressions that relate influence factors in the measurement procedure to the final measurement result [28]. Each influence factor will have a corresponding parameter within the model. In the case of coordinate measurement systems, the model parameters correspond to the behaviours of the various mechanisms that allow the instrument to make a coordinate measurement. For example, contact-probe CMMs make three-dimensional measurements by translating a touch-probe along mechanical axes. In an ideal Cartesian system, the axes are orthogonal to each other and do not exhibit any positioning, straightness, or tilt errors [29]. Assuming no environmental factors, *e.g.* temperature variations from the specified reference (usually 20 °C) or vibrations, the model of such an ideal system would simply be defined by a Cartesian coordinate system with inputs X, Y, and Z, corresponding to the position along each translation axis. The surface coordinates of a sample (the output) would be a collection of the input coordinates for each probing point. However, in practice, mechanical axes can have myriad error motions. In the presence of these motions, the actual position of a touch probe deviates from the intended position. In order to map the behaviour of the mechanical axes, parameters that correspond to the possible error motions are introduced in the CMM model. Once the error motions have been experimentally measured, the parameters in the measurement model are populated with their corresponding quantities. If the measurement model accurately describes the behaviours of a specific

6

test system, the results of a simulation should be very close to the results that the test system would provide given the same measurement task. The difference between model output and test results is often used as criteria to evaluate how well the model describes a test system. Measurement models have also been applied to laser trackers [30] and laser scanners [31].

XCT is an imaging technology and, as such, an XCT model is an imaging model. In particular, concepts from projective geometry are applicable in describing how X-rays are projected from the source, through the sample, and onto the detector [1]. The geometrical relationships between the three main components of an XCT system are incorporated into the parameters of a projective geometry model. Given a set of geometrical parameters, the model maps the three-dimensional space of the sample onto the two-dimensional radiograph for each rotation position or 'pose' of the system. However, due to the fact that XCT systems also incorporate kinematic parts, the imaging model needs to allow for changes in geometry as a result of changes in the kinematic configuration. Therefore, the mechanical models and principles often used in modelling CMMs are applicable to XCT systems together with projection models [32].

One of the benefits of having a measurement model is the ability to evaluate the sensitivity of a measurement to each influence factor. Such a study can be performed either by analytical derivation of the mathematical expressions relating the measurement output to each influence factor [33] or by performing simulations in which the measurement results are observed as the various parameters are changed [34]. A model can also be applied to determine the influence quantities of a test system. In this method, the model is fit to a set of experimentally observed results; the parameters in the model are allowed to change until the simulated results resemble the observed results. In this section, the application of models to sensitivity studies will be discussed. The 'inverse' application of the model to determine influence quantities will be covered more thoroughly in section 5.1 on imaging methods.

A previous study [35] simulated the effects of tilts and positioning errors on the measurement of sphere-to-sphere distances for ball bars of various lengths. In this study, an error model was developed to consider errors in the Z positions of the X-ray source, rotation stage and detector. The error model also incorporates angular errors of the detector, such as tilt, slant and in-plane rotation. The ball bars were measured in different regions of the detector and at different orientations. The value of each error parameter was controlled individually and the effect on sphere-to-sphere distances was observed.

Results from the simulation indicate that certain error sources affect measurement error more strongly than others. Figure 5 shows the measurement error on a 2 mm ball bar as a function of errors in the positioning of source (a), rotation stage (b), and detector (c). Errors in source and rotation stage positioning had a larger effect on measurement error than positioning errors of the detector. This difference in sensitivity is noted by the fact that, in order to attain the same measurement errors, the largest detector positioning error is thirty five times larger than both source and rotation stage positioning errors. The study found that measurements made at high magnification (smaller voxel size) were more sensitive to positioning errors than measurements made at low magnification (larger voxel size). The sensitivity is evaluated as the ratio of measurement error to voxel size. A source positioning error of 100 μm resulted in a 0.5 % length measurement error. Rotation stage positioning errors of 100 μm also resulted in a length measurement error of 0.5 %. An error in detector positioning of 3500 μm yielded a 0.0035 % length measurement error, which is well below the noise level of general XCT measurements. The plots also indicate that measurement errors due to positioning errors did not have a strong dependence on ball bar orientation and position in the area of the detector. This is shown

by the overlapping of the different plot lines. Thus, it can be deduced that positioning errors result in global scaling errors throughout the measurement volume.
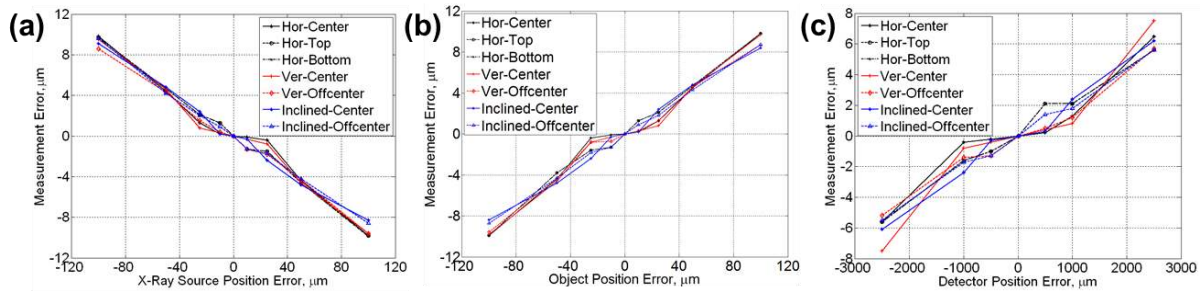

Figure 5. The error in measuring a 2 mm ball bar at various positions and orientations is plotted as a function of (a) X-ray source position error, (b) object position error and (c) detector position error. Figures from reference [35].

Errors in the angular orientation of the detector were also simulated. Figure 6 shows errors in measurement of a 2 mm ball bar as a function of in-plane rotation (a), tilt (b) and slant (c). The maximum in-plane rotation (0.4°) results in length measurement errors up to 0.1 %. The plot shows that errors from in-plane rotation increase as the ball bar is positioned away from the centre of the detector. The presence of detector out-of-plane tilt has a significant effect on the measurement of vertical lengths and very little effect on horizontal lengths. The opposite is true for detector slant; horizontal lengths were measured to have higher errors than vertical lengths. For both tilt and slant, misalignments of 10° resulted in errors up to 1.5 % of the measured length, depending on the position and orientation of the ball bar. The author explains that in-plane rotation can be easily corrected by software and is, therefore, not a critical alignment. On the other hand, the author suggests that detector tilt and slant should be aligned to within 1° to 2° from nominal.
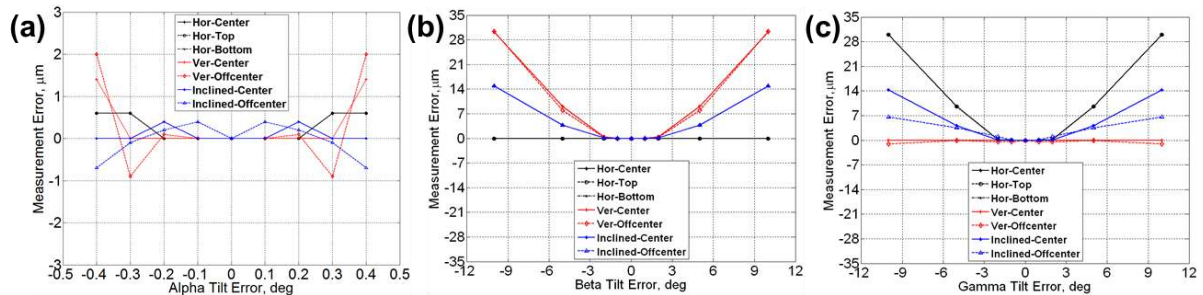

Figure 6. The error in measuring a 2 mm ball bar at various positions and orientations is plotted as a function of detector (a) in-plane rotation, (b) tilt and (c) slant. Figures from reference [35].

Another study [36] also simulated the effects of geometrical errors on a reference object. In this study, the authors observed the effects of detector tilt, slant and in-plane rotation. Each of the angles was individually offset by 1° from their ideal alignment. The average measurement error for a set of seven dimensional features on an alloy object (figure 7) was observed as a result of each misalignment separately. The results show that in-plane rotation of the detector caused the largest average error in the measurement of the seven features (about 3.5 % relative measurement error). The errors as a result of detector tilt and slant were barely noticeable.

8

The authors also looked at the influence of misalignments in the rotation axis of the rotation stage. The seven features on the same object were measured and the influence of each error source was determined. A lateral shift of the rotation axis along the X-axis of 700 μm, which corresponded to a shift of two pixels on the detector, led to an average relative measurement error of about 2.5 %. A 1° tilt of the rotation axis about the X-axis resulted in a relative measurement error of about 0.5 % over all features of the object.
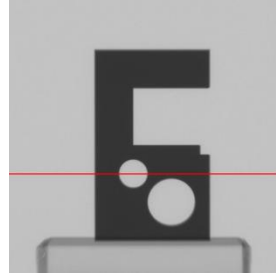

Figure 7. A study [36] simulated the influence of detector tilt, slant, and in-plane rotation, as well as tilt and lateral offset of the rotation axis on the measurement of seven features of a simulated object. Figure from reference [36].

It is interesting to compare the results of detector misalignment in this study to the results shown in reference [35]. In reference [36] it is concluded that, for equal angle misalignment of 1°, in-plane rotation had the largest effect on measurement error. On the other hand, the simulation study in reference [35] limits the in-plane rotation to 0.4° while changing tilt and slant by 10°. It is then concluded that tilt and slant have larger effects on measurement error than in-plane rotation. It should be noted that the authors of reference [35] reason that in-plane rotation is easily correctable by software means and, therefore, does not pose a critical issue in geometrical alignment. Also, the test object in reference [36] includes various dimensional features (outer edges, inner edges, circle-to-circle distance, and circle diameter), whereas reference [35] performed the simulation on a ball bar at various orientations and positions. It is important to note that the measurands in reference [36] suffer from edge offsets, which are caused by thresholding errors. The measurands in reference [35], on the other hand, do not suffer from edge offsets [37]. It should be noted that the observations made on the sensitivity of measurement error to various error sources are highly dependent on the measurement setup (*e.g.* magnification position, pixel size).

5   METHODS TO DETERMINE GEOMETRICAL INFLUENCE FACTORS

In the literature, the methods to determine the geometry of XCT systems can be divided into two categories. The first category considers the geometry for a fixed kinematic position of the rotation stage. In these methods, a reference object is imaged and the imaging geometry is deduced from the projection data, *i.e.* the radiographs, or from the voxel data (in the case of scale correction). These methods are accordingly referred to as 'imaging methods' in this review. Some imaging methods consider the behaviours of the rotation stage as a function of rotation position as well as drifts of the X-ray focal spot. However, the imaging methods found in the literature are only applicable for limited (if not fixed) positions of the rotation stage; if the kinematic position of the rotation stage is changed, the geometry must be newly evaluated. For this reason, the second category of methods in the literature considers the error motions of the kinematic assembly. These methods are based on the use of reference instruments, such as laser interferometers and electronic levels, to measure kinematic behaviours. The structure of section 5 is given in figure 8.
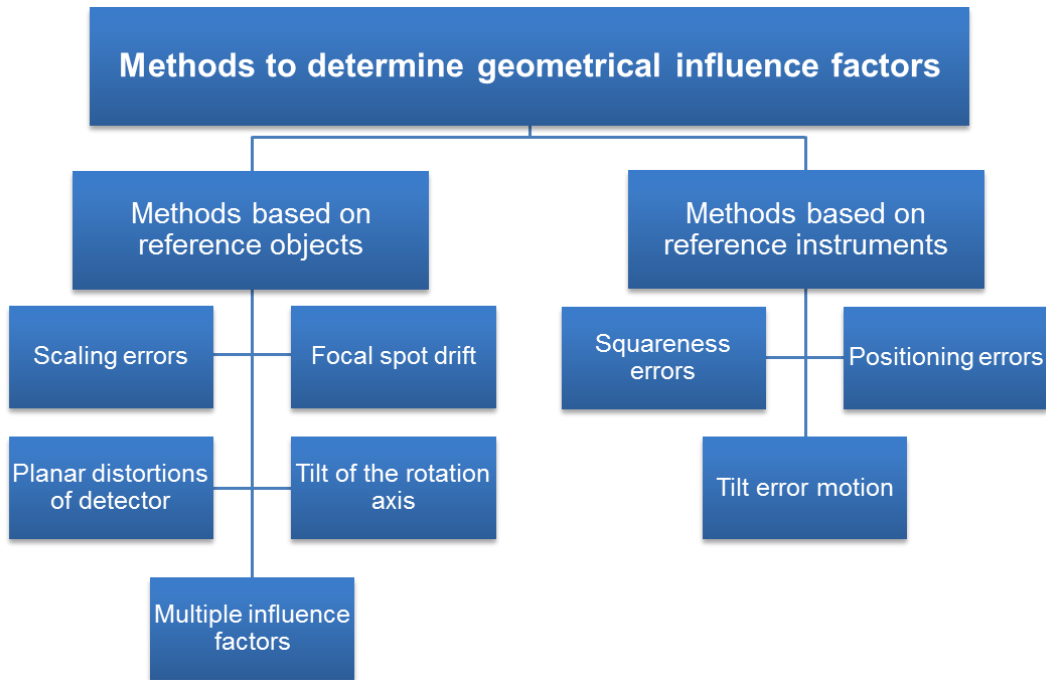
Figure 8. The methods to determine geometrical influence factors are separated into two categories: methods based on the use of reference objects (also known as imaging methods) and the methods based on the use of reference instruments.

5.1 METHODS BASED ON REFERENCE OBJECTS

The general principle of imaging methods is the analysis of radiographic or voxel data to evaluate system geometry. Most imaging methods consist of imaging reference object(s) placed in the instrument's field of view. There are some imaging methods that do not require a dedicated object [38–49]; these methods are often known as 'on-line' methods. The guiding principle behind 'on-line' methods is the improvement in image and reconstruction quality rather than determining dimensional accuracy. Still, the methods discussed in references [38–49] can provide insight into geometrical calibration of XCT systems. However, for purposes of conciseness, only imaging methods that utilize dedicated reference objects will be covered in this review.

In general, imaging methods take advantage of concepts from projective geometry. A projective imaging model describes the relationship between the three-dimensional coordinates (x, y, z) of an object placed in the system's field of view and the coordinates of its projected image (1D for fan-beam XCT and 2D for cone-beam CT). This relationship is dependent on the geometry of the imaging system. Imaging methods exploit this dependence to inversely determine system geometry from projection data, given some *a priori* information about the object or the system. It should be noted that some studies presented here were developed for single-photon emission computed tomography (SPECT) systems; this is of no consequence since the principles presented are also relevant to XCT systems. Also, in this section both simulation and experimental studies are presented; the order in which the literature is presented does not separate the two types of studies. Thus, the topics will alternate frequently between simulation and experimental studies.

In section 5.1.1, methods dedicated to determining scaling errors, *i.e.* errors in the magnification, are presented. Methods to determine drift of the X-ray focal spot are presented in section 5.1.2. Planar distortions of the detector are covered in section 5.1.3. The determination of rotation axis tilt is presented

in section 5.1.4. Finally, section 5.1.5 is dedicated to a particular set of studies designed to determine various parameters in the system geometry. The studies in section 5.1.5 are overwhelmingly from the field of medical physics, in which the systems often employ a rotating gantry about a fixed stage. Nevertheless, the methods provide insight into future development of procedures for industrial XCT systems.

5.1.1 Scaling errors

It is appropriate to start the discussion with those methods that have been widely accepted by researchers in the field of industrial XCT [1]. A common procedure is to compensate for errors between registered and effective magnification factor, *i.e.* the ratio of *SDD* and *SRD*. The general practice for these 'scale correction' methods is to scan a reference object, which has a series of calibrated length segments, and to subsequently re-scale the voxels given the difference between the lengths measured by XCT and their corresponding calibrated values. In reference [6], a carbon-fibre plate with twenty five ruby spheres arranged in a regular grid pattern is used as a reference object (figure 9a). The distances between sphere centres (for all possible sphere pairs) were calibrated on a reference instrument. Subsequent to scanning the reference object and performing volumetric reconstruction, the distance between each pair of sphere centres is measured by XCT. The authors calculate the deviation (measurement error) of each XCT length measurement from its calibrated reference value. The collection of sphere distance errors are plotted against their corresponding calibrated values in figure 9b. A linear regression fit is applied to the sphere distance errors and the slope of the fit line, *a*, is used to correct the voxel scale *via* equation 1

$$s_{vox} = \frac{1}{a+1},$$ (1)

where *a* is the slope of the sphere distance error data and s_{vox} is the correction factor to be applied to the original voxel scale. The voxels were consequently corrected and the residual sphere distance errors were plotted against their corresponding calibrated values (figure 9b). The effect of the scale correction procedure is noticeable in the residual sphere distance errors.
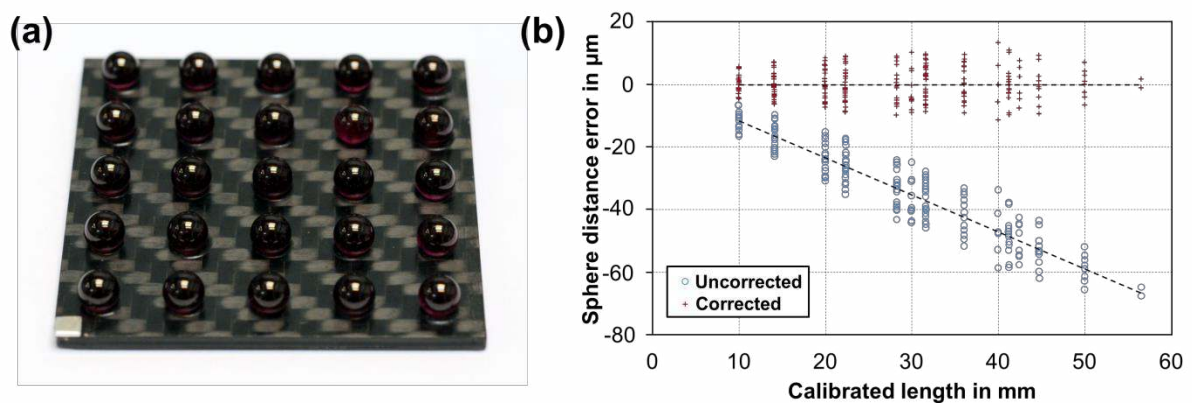

Figure 9. (a) A ruby sphere plate is used as a reference object for compensating errors in effective magnification factor. The centre-to-centre distances between spheres (sphere distance) are calibrated on a reference instrument. (b) The error in sphere distance is plotted against the corresponding calibrated length. The slope of the plotted errors is used to correct the voxel scale. Figures from reference [6].

Other studies [50–56] on scale correction methods were performed and were based on the same principle of recalculating voxel scale from the measurement of calibrated features on a variety of reference objects. In reference [50], the authors performed scale correction multiple times over a period of a few months and observed a change in scale correction factor. For this reason, and due to poor repeatability in the positioning of the rotation stage2, the authors recommend that the scale correction methods be carried out either immediately before or immediately after the test scan. On the other hand, if the kinematic positioning is shown to be stable over time, then repeated scale correction might not be necessary. Additionally, instabilities in the position of the X-ray source (focal spot drift) during a scan result in a drift of the effective magnification factor between radiographs. This change in scale between radiographs can be detrimental to the quality of the reconstructed volume. The measurement of focal spot drift is covered in section 5.1.2.

Scale correction is shown to provide significant improvement in measurement error. However, because of poor repeatability in the kinematic assembly of the system, it is necessary to perform scale correction for each test measurement. It should be noted that the studies mentioned so far apply an error correction to the entire volume of the model, that is, a correction to the effective magnification factor. Dimensional errors can also be non-uniform, *i.e.* they differ from voxel to voxel. In reference [56] a clear difference is shown in dimensional errors along a vertical cross section of the volumetric model. The authors measured a stack of spheres oriented vertically (figure 10a). The sphere-to-sphere distance is measured for each pair of adjacent spheres and the error in distance is plotted against reference values (figure 10b). The trend in measurement error for subsequent sphere distances confirms that a systematic non-uniform error exists along the vertical cross section of the volumetric model.
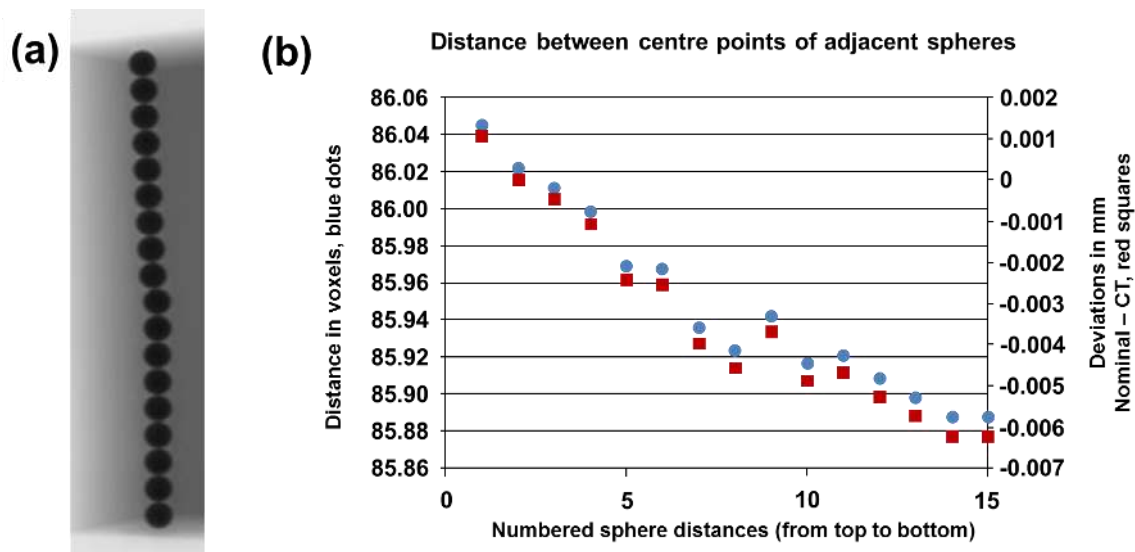

Figure 10. (a) A vertical stack of spheres was imaged and the sphere distance between adjacent spheres was compared to the reference measurement. (b) A clear trend in the measurement error as a function of vertical position in the volumetric model confirms the existence of non-uniform errors. Figures from reference [56].

Non-uniform errors can exist as a result of various factors, including tilt and slant of the detector, tilt of the rotation stage about the horizontal axis, and distortions along the detector plane (such as dissimilar

---

2 Note: This is discussed in more detail in section 5.2.

pixel sizes). In the presence of non-uniform errors, a simple scale correction procedure does not suffice [35].

5.1.2 Focal spot drift

Efforts are ongoing in the research community to characterize drift in the focal spot [27,57–60]. These characterization studies often involve observing the drift in the projection of a reference object placed close to the X-ray source. The position of the object at high magnification allows small drifts to be observed; however, penumbral effects due to the finite focal spot size are a setback at high magnifications. In reference [59], focal spot stability was observed as a function of X-ray tube heating. The authors reason that, while most X-ray tubes have an internal cooling mechanism, not all sources of heat are accounted. In particular, heat from the objective coils and objective aperture (see figure 11a) contribute to an expansion of the entire X-ray tube assembly. The test procedure involved measuring the expansion of the X-ray tube with an indicator (figure 11b) as a function of operation time. Simultaneously, the authors observed the drift in the projection of a crosshair positioned at a high magnification position. Tests were performed with and without additional cooling from an external module to compensate for the unaccounted sources of heat in the X-ray tube. Results from the test on the X-ray tube without external cooling are shown in Figure 12a. In this plot, the thermal expansion of the X-ray tube and the drift of the crosshair projection are closely correlated. After two hours of X-ray gun operation, both drifts reach values of around 30 μm. In figure 12b, the results from the externally-cooled X-ray tube are presented. The application of external cooling provides a clear reduction of the observed expansion and projection drift. Both thermal expansion and crosshair position stay relatively stable over the period of two hours. It should be noted that the correlation between thermal expansion of the X-ray gun and focal spot drift in figure 12a might not be present for all systems. In particular, some systems the X-ray target is bolted to the frame of the instrument, meaning that thermal expansion of the tube does not result in a drift of the target. However, focal spot drift can still occur due to instabilities in the electron beam.
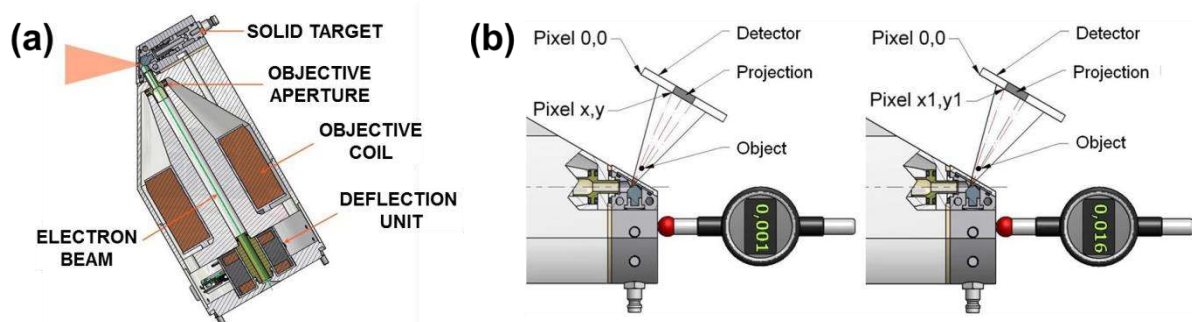

Figure 11. (a) Heat from the objective coils and objective aperture of the X-ray tube can result in thermal expansion of the X-ray tube assembly. (b) The physical expansion of the X-ray tube was measured with an indicator as a function of operation time. Simultaneously, the drift of a highly magnified crosshair projection was observed. These tests were performed on the X-ray tube with and without external cooling. Figures from reference [59].
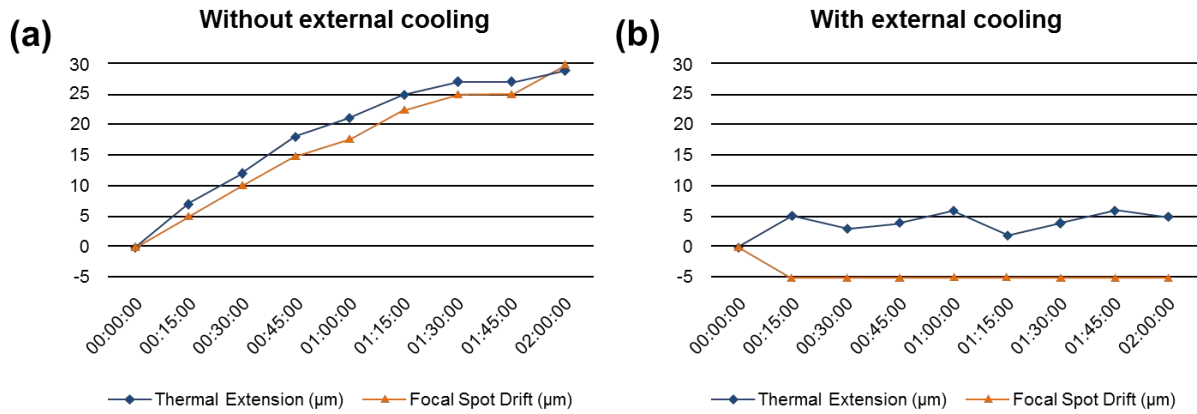
(a) Without external cooling and **(b) With external cooling** — plots of Thermal Extension (µm) and Focal Spot Drift (µm) versus time from 00:00:00 to 02:00:00.

Figure 12. (a) Results from the test without external cooling show continuous expansion of both X-ray tube and crosshair projection (denoted 'focal spot drift' in reference [59]). (b) Results with external cooling of the X-ray tube clearly demonstrate a reduction in both thermal expansion and projection drift. All values along the vertical axis of the plots are in micrometres. Figures from reference [59].

5.1.3 Planar distortions of detector

Geometrical distortions in the plane of the detector were investigated in reference [61]. A calibrated grid reference object was imaged at various in-plane detector rotations. The authors observed reproducible geometric distortions in the plane of the detector. Detector distortions are mapped in figure 13. The authors claim that the observed distortions were not a result of temperature effects. To validate their observations, the authors imaged a calibrated test object at different vertical positions within the plane of the detector. The object consisted of several spheres, the distances between which were calibrated on a reference instrument. Length measurement errors were evaluated with and without corrections for the observed distortions. The error in sphere-to-sphere distance is shown to be consistently smaller at each position in the detector after distortion correction was applied (figure 14). The authors argue that detector distortions could result from errors in the manufacturing process of flat-panel detectors or from internal light guiding of the scintillating crystals.
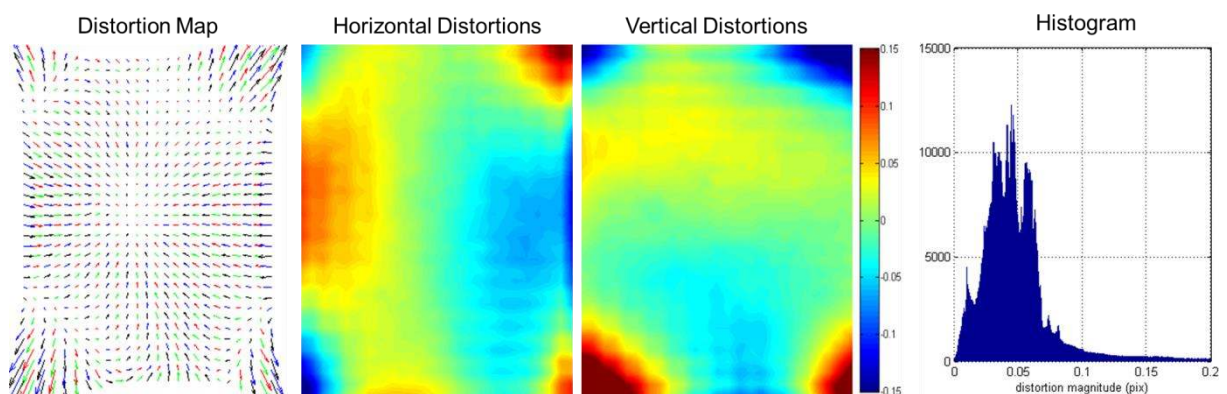

Figure 13. A grid-like object was imaged at various detector in-plane rotation angles and reproducible geometric distortions were observed in the plane of the detector. The left image is a vector representation of the geometric distortions, while the centre two images show horizontal and vertical distortions, respectively. The values on the colour bar are in pixels [61]. The right image is a distortion histogram. Figures from reference [61].
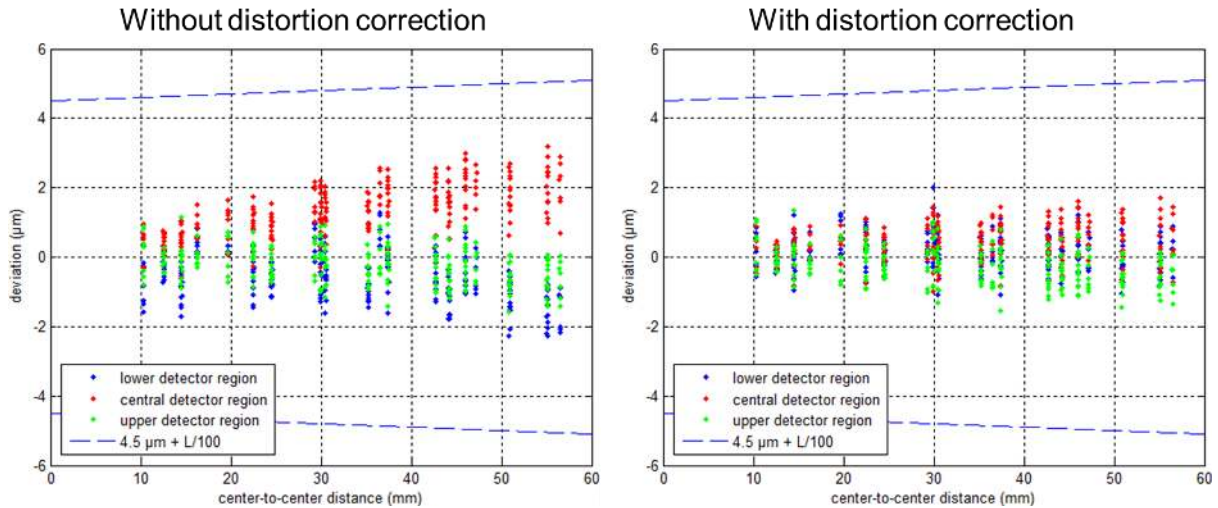
14

Figure 14. The measured sphere distance errors on the test object were evaluated with and without correction for the observed detector distortions. The errors after distortion correction were consistently smaller [61]. Figures from reference [61].

In another study [62] the author argues that methods to determine detector distortion based on grids (or other objects with regularly distributed features) provides a sparse sampling of the detector. The author therefore presents a method to evaluate 'fine' irregularities in a linear detector for fan-beam CT; it should be noted that the author provides suggestions for the extension of the method to cone-beam systems. In particular, the method seeks to determine the spatial position of each pixel with respect to the projection of the rotation axis on the detector; in the literature, the term iso-ray is used to denote the X-ray path from the source to the detector and intersecting the rotation axis. A pin is imaged at up to eight thousand rotation positions within a full revolution. When the centre of the pin falls on a given pixel, the corresponding rotation position is used to evaluate the location of the pixel, which is given by the angle γ from the iso-ray (figure 15a). Within a full revolution of the rotation axis, each pixel should be sampled twice.
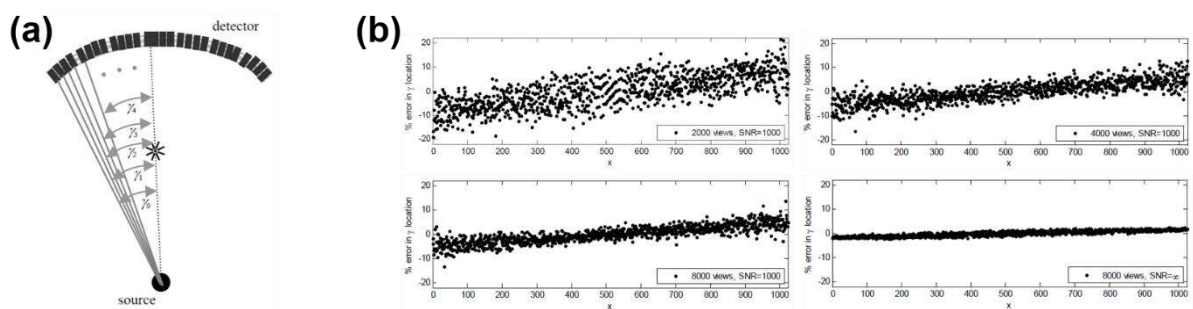

Figure 15. In reference [62], spatial irregularities of detector pixels are evaluated by way of imaging a pin at 2000, 4000, and 8000 positions within a full revolution of the rotation stage. (a) Pixel position of a curved linear detector (fan-beam CT) is described by the angle γ between the ray connecting the source to the pixel and the iso-ray. (b) The method was simulated and the results were compared to the parameters of the imaging model. The error in determining pixel position is plotted as a percentage of the mean spacing between adjacent pixels. More rotation positions results in lower variation in the measurement errors. Figures from reference [62].

15

The effectiveness of the method was tested by simulation with varying numbers of rotation positions: 2000, 4000, and 8000. Additionally, the method was tested with and without Gaussian noise in the pixel grey values. Figure 15b shows the error of the simulated method in determining pixel position when compared to the actual pixel positions in the model. The error is presented as a percentage of the mean spacing between adjacent pixels in the model. It is clear from the data that an increase in rotation positions results in more consistent error values. As can be expected, the results without noise exhibit the smallest error. The slope in the plots corresponds to a scaling error in the determination of the mean spacing between adjacent pixels (evaluated from coarser measurement procedure). It should be noted that this method relies strongly on the stable motion of the rotation axis and the accuracy of its angular encoder.

5.1.4   Tilt of the rotation axis

In general, rotation axis tilt about the Z axis is treated as an in-plane rotation of the detector η. The detector's in-plane orientation is considered aligned when its columns are parallel to the direction of the rotation axis. Therefore, the orientation of the rotation axis about the Z axis is actually used as the reference for aligning the detector. On the other hand, tilt of the rotation axis about the X axis must be considered independently from the detector. In reference [63], the evaluation of this tilt for input into the simulation model is discussed. The authors suggest that, in the absence of a tilt about the X axis, the projection of a point object located on the mid-plane will occupy the same v coordinate on the detector as it is rotated (figure 16a). However, in the presence of such a tilt, the projected point object will traverse multiple v coordinates as it is rotated (figure 16b). The authors estimated tilt of the rotation axis by imaging the contact point between two spheres (figure 16c) at multiple rotation positions and performing trigonometric analyses on its projected coordinates.
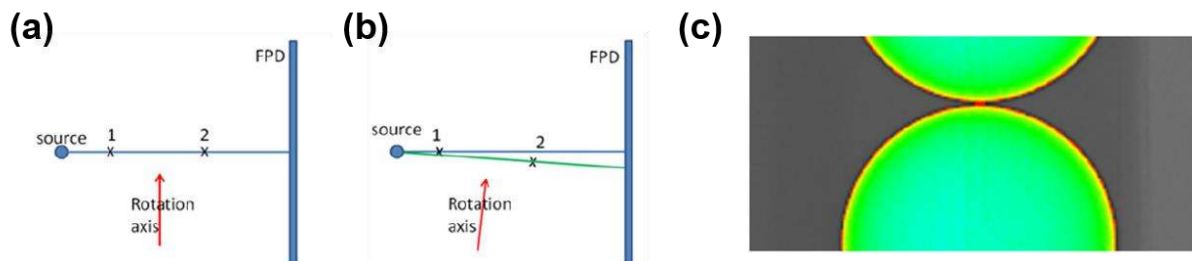

Figure 16. The authors of reference [63] describe the principle behind their method of evaluating rotation axis tilt about the X axis. (a) In the absence of this tilt, the projection of a point object located on the mid-plane will occupy the same v coordinate on the detector as it is rotated. (b) If the rotation axis is indeed tilted, the projected point object will traverse multiple v coordinates as it is rotated. (c) The contact point between two touching spheres is used as the point object in the test. Figures from reference [63].

In reference [64] an imaging method to determine tilt about the X-axis θ_r is presented. A 'block' consisting of Vernier structures on two opposing sides (figure 17) is used as a reference object. Each Vernier structure consists of two line scales with different periodicity. At one point along the length of the Vernier structure, two graduations (one from each scale) coincide. The position of this coincidence is the feature of interest for both Vernier structures. A linear grid is also added for determining tilt of the rotation axis with respect to the detector columns (detector in-plane rotation). The block is imaged at two rotation positions 180° apart. At each rotation position, the detector row value of the projected feature for each structure is noted and the difference in the value between the two Vernier structures is calculated. The two difference values (at 0° and 180° rotation positions) are used to calculate the tilt of

the rotation axis about the X-axis. Unfortunately, the study did not provide an evaluation of the method's accuracy in determining this tilt.
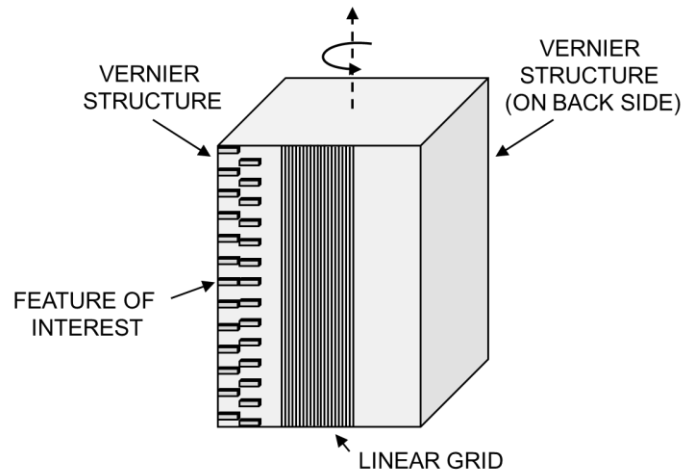

Figure 17. Vernier structures and a linear grid are incorporated into a 'block' reference object. The linear grid is used to determine in-plane rotation of the detector, while the Vernier structures are used to determine rotation axis tilt about the X-axis. Figure adapted from reference [64].

5.1.5   Multiple influence factors

The imaging methods in this section are overwhelmingly from the field of medical physics. In general, these methods are based on reference objects consisting of one or more circular or spherical markers. The centres of the spherical markers are used to represent point coordinates in both the 3D object space and on the projected image. The term 'point markers' will be used to denote such markers. Most reference objects consist of a particular arrangement of point markers. Reference objects consisting of several roughly positioned markers, often in an approximately linear array, provide a simple solution to the problem since they don't require precise alignment. However, the disadvantage of these simple methods is the reliance on assumptions with regards to the system geometry. For example, most of the imaging methods based on simple reference objects require projections to be taken at various rotation positions. An assumption that is often made is that the rotation axis is perfectly stable, *i.e.* no tilt or positioning error motions as a function of rotation angle. Other imaging methods, on the other hand, employ reference objects with a structured arrangement of point markers, *e.g.* circular orbits and orthogonal structures. The advantage of these methods is the ability to determine system geometry from one rotation position, thereby avoiding assumptions on the rotational stability. In fact, these methods can be applied to evaluate system geometry as a function of rotation angle and, subsequently, to characterize instabilities in the rotation.

Methods based on imaging of point markers can be distinguished by the process with which the geometrical parameters are determined from projection data. Two of the more prominent processes are numerical optimization (also known as iterative fitting) and analytical evaluation (also known as direct determination). Numerical optimization methods determine geometrical parameters by way of iteratively fitting simulated projections from an imaging model to the observed projections from a test system. A cost function is defined as the difference between simulated and observed projection coordinates. As the parameters of the imaging model are iteratively changed, the value of the cost function will also change. When the cost function is minimized, the parameters of the imaging model should be closest to those of the test system. A shortcoming of optimization methods is the presence of

local minima in the cost function; in this case, the minimization of the cost function has been satisfied but the resolved set of parameters might not be representative of the test system. Thus, to ensure an accurate solution, it is essential that the initial parameter values in the model be reasonably close to the true values. This can be achieved by first obtaining rough estimates of some or all of the parameters by other methods. Alternatively, analytical methods determine geometrical parameters by directly solving a set of equations that relate projection data to the system geometry. Analytical methods do not suffer from the shortcomings encountered in optimization methods. However, analytical methods often require *a priori* information about the reference object or about the system geometry.

It should be noted that the methods in this section are not organized by the type of analysis performed. Instead, the studies are presented in the context of the error parameters considered in the proposed methods. The first studies are based on imaging a reference object at limited positions and rotations of the stage. The second category of studies consists of methods based on the circular, that is, ideal, rotation of the stage. Finally, methods that consider rotational instabilities of the stage are presented.

Methods based on fixed or limited positions of the rotation stage

One of the earlier studies [65] proposes a set of procedures to analytically determine misalignments and offsets in cone-beam systems using a grid-plate with regularly distributed holes. Each hole is identified sequentially by a number $i = 1$ to N (figure 18a). When the grid is imaged, the centre of each projected hole P_i is denoted by (u_i, v_i) in the coordinate frame of the detector (figure 18b). One of the first steps in aligning the system involves ensuring that the magnification axis is centred on the detector. To resolve the principal point, the grid-plate is imaged at two magnification positions (figure 18c). The normal to the grid plate should be parallel to the Z axis; this assumes the magnification and Z axes are roughly parallel to each other. As the grid-plate is moved from the first magnification position to the second, the pixel coordinate of each hole will move from $P_{i,1}$ to $P_{i,2}$. By definition, the projection of the X-ray source will not experience a change in pixel coordinates between magnifications. The authors provide an equation for calculating (u_o, v_o) from the set of hole coordinates $P_{i,1}$ and $P_{i,2}$.
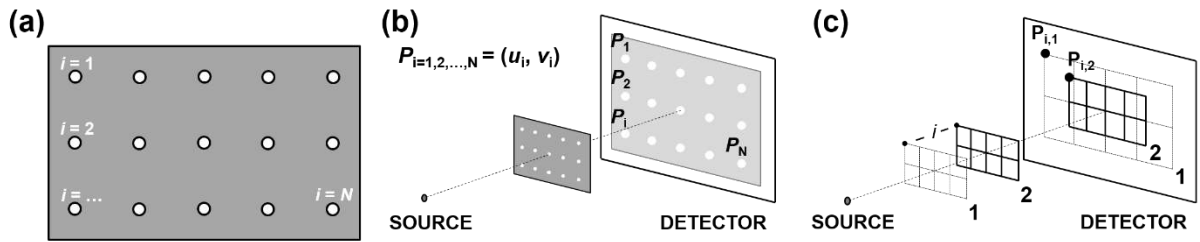

Figure 18. (a) Misalignments are determined in reference [65] by way of imaging a grid-plate with regularly distributed holes. Each hole is assigned an identifier i from 1 to N. (b) The projection of each hole is assigned an identifier P_i, where the subscript i corresponds to the respective hole identifier on the grid-plate. (c) The principal point of the system can be determined by imaging the grid-plate at two magnification positions. The authors provide a mathematical relationship between the principal point and pixel coordinates of the imaged holes at multiple magnifications. Figures adapted from reference [65].

In an ideal system, the rotation axis of the stage is parallel to the columns of the detector. An angular deviation of the rotation axis about the normal to the detector is equivalent to an in-plane rotation of the detector η. To determine the in-plane rotation of the detector, the grid-plate is imaged at two rotation angles 180° apart. The projected hole centres at the 0° and 180° position are identified as $P_{i,0}$ and $P_{i,\pi}$, respectively. Again, the grid-plate is positioned such that its normal is parallel to the Z axis at the 0°

position. If the rotation axis is parallel to the detector columns, the v coordinate of each imaged hole will remain the same between rotations, *i.e.* $v_{i,0} = v_{i,\pi}$. If this is not the case, a mathematical relationship is provided to calculate the tilt between the axis of rotation and the detector columns (figure 19a). Also, the rotation axis should ideally intersect the magnification axis, *i.e.* the projection of the rotation axis should intersect the principal point on the detector plane. The grid-plate is imaged at two rotation angles 180° apart (figure 19b). For each hole, the centre of mass between the two rotation positions along the U axis, $u_{i,0}$ and $u_{i,\pi}$, is calculated. The U position of the rotation axis, u_r, is given by the average centre of mass of all hole centres. If the rotation axis indeed intersects the principal point, then u_r should be equal to u_o. Otherwise, the rotation axis is offset from the magnification axis.
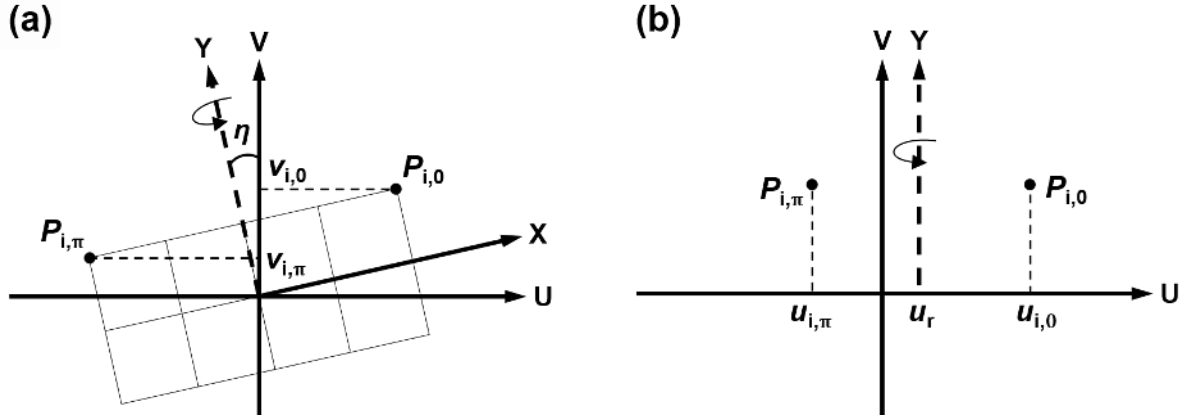

Figure 19. (a) A tilt of the rotation axis about the normal to the detector can be determined by imaging the grid-plate at 0° and 180° rotation positions. The relationship between corresponding pixel coordinates for each hole can be used to determine in-plane rotation, η. (b) Similarly, an offset of the rotation axis from the magnification axis can be determined by imaging the grid-plate at 0° and 180° rotation positions and performing analyses on the projected hole coordinates. Figures adapted from reference [65].

The authors of reference [65] provide a way of calculating *SRD* from pixel coordinates of the hole centres at two or more known magnification positions. If two magnification positions are used, the principal point must be known in addition to the distance between the two positions. If three magnification positions are used, only the distance between the positions is necessary. Additionally, pixel size (the term 'sampling step' is used in the study) can be calculated from the known hole-to-hole distances.

The study in reference [65] also evaluates geometrical distortions in the plane of the detector. The method involves imaging the grid-plate parallel to the plane of the detector and fitting polynomial functions to the projection of the grid. Any distortions in the plane of the detector will result in distortions of the structure in the projected grid. Global distortions are fit by quadratic equations, whereas local distortions are fit by higher-order polynomial equations for each triangular area defined by lines connecting three adjacent holes.

Another purely analytical method is proposed in reference [66] using a square plate with four point markers at each of the four corners (figure 20). The length between two point markers l is measured in advance. The authors convert offsets and misalignments in the X-ray source and rotation axis to a set of six parameters in the detector coordinate frame. Analytical expressions are provided that describe the conversion of X-ray source position errors (Δx_s, Δy_s, Δz_s), rotation axis position errors (Δx_r, Δy_r, Δz_r), rotation axis tilt about the X-axis θ_r, and rotation axis skew η_r (about the Z-axis) to the "global" error

parameters in detector position (Δx, Δy, Δz) and detector orientation (θ, φ, η). Additionally, consideration is given to the fact that detector tilt, slant and in-plane rotation may not be centred along the middle row, column, and pixel, respectively. Despite the fact that rotation axis tilt and skew are considered, the authors suggest aligning the rotation axis prior to performing the parameter evaluation. The method involves first evaluating the two out-of-plane rotations of the detector θ and φ then calculating Δz. Given the calculated parameters, the detector coordinates are tilted and twisted accordingly to compensate for the out-of-plane rotations. Additionally, the coordinates of the detector are modified to account for Δz. The rotated and translated coordinates are then used to evaluate the in-plane rotation of the detector η. Finally, Δx and Δy can be evaluated.
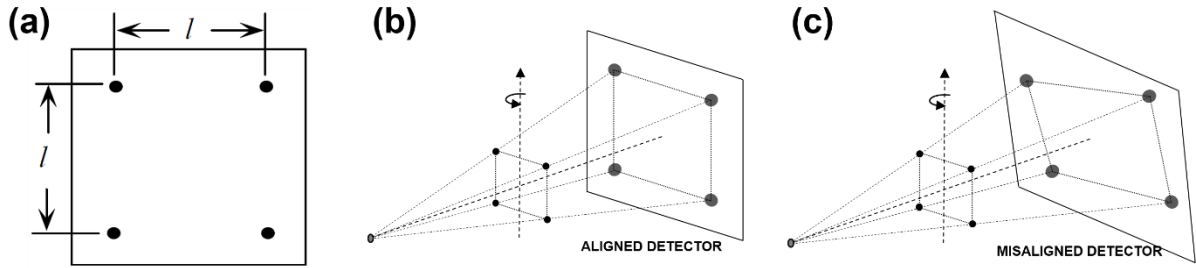

Figure 20. In reference [66], the system geometry is defined by a set of six detector parameters. (a) A square plate with four embedded point markers is proposed as a reference object. The point markers are positioned at each of the corners of the plate. (b) In the case of an aligned detector, the line segments between point markers will form a square. (c) Any misalignment in the detector will result in the line segments being imaged in a non-square arrangement. Figures from reference [66].

The quality of parameter estimation is determined by simulating the method on several misaligned geometries. In the first simulation, the authors applied misalignments to the X-ray source position, while keeping the rotation axis and detector perfectly aligned. The simulation was performed similarly for misalignments in the rotation axis position and detector. Then, a second set of simulations held one component aligned while applying misalignments to the other two components. A final simulation applied misalignments to all three components. Given the analytical expressions relating X-ray source and rotation axis misalignments to the detector misalignments, the authors provide the equivalent misalignments of the detector when misalignments are applied to the other two components. According to the results, the lateral positioning offsets Δx and Δy and in-plane rotation of the detector η were determined accurately for every combination of misalignments. On the other hand, the estimation accuracy of Δz, θ, and φ differed depending on the applied misalignments. The largest estimation error in Δz (0.132 mm), θ (0.3154°), and φ (0.1408°) occurred for the simulation in which both source and detector were misaligned. Large errors are observed in the estimation of out-of-plane detector rotations θ (-0.2412°) and φ (0.1267°) for the simulation in which all components were misaligned. It is interesting to note that, for the same simulation, there were no errors in the estimation of Δz.

It should be noted that the previous results were evaluated for perfectly acquired point projection coordinates. The authors investigated the effects of errors in the point projection coordinates on parameter estimation. In the simulation only detector misalignments were applied since the method was able to evaluate the parameters exactly. The coordinates of each projected point marker were systematically perturbed by 1/10, 1/3, 1/2, and 1 pixel(s) sequentially. At each pixel perturbation, the parameters were evaluated. The error in estimating out-of-plane rotations degraded substantially with increasing point coordinate errors. An error in point coordinates of 1 pixel yielded estimation errors of 0.3798° in θ and -0.3246° in φ. The errors on other parameters were negligibly small. The authors of reference [66] applied the results of their parameter estimation procedure to modify the reconstruction algorithm in a subsequent study [67]. In this study, it was found that translational errors and in-plane rotation of the detector affect reconstruction quality more severely than out-of-plane rotations.

Methods based on ideal rotation of the stage

In these studies, reference objects consisting of one or more point markers, *e.g.* small spheres or ball bearings, are imaged at multiple rotation positions. The methods are designed with the assumption that the rotation stage behaves ideally. Early studies [68,69] evaluate system geometry by imaging a single point marker at various angular positions of the rotation stage (figure 21); the authors apply numerical optimization methods. In reference [68] the procedure is presented for a fan-beam system defined by the parameters *SRD*, *SDD*, principal point, and X-offset of the rotation axis from the magnification axis *m*. This method was subsequently adapted to a cone-beam system in reference [69]; in this study on a cone-beam system, the axis of rotation is assumed perpendicular to and coincident with the magnification axis, therefore the geometry is defined by *SRD*, *SDD*, and the principal point.
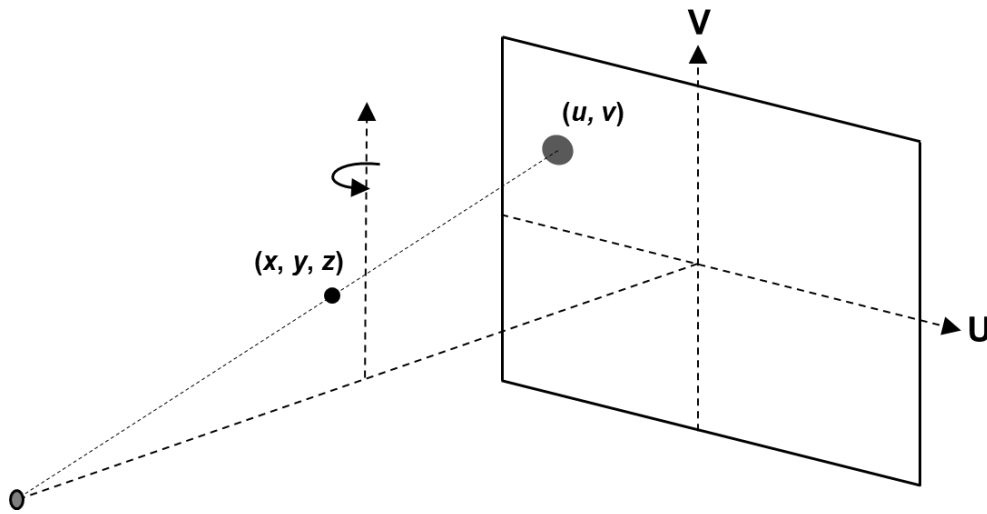

Figure 21. Projective geometry is used to model the projection of a point marker from three-dimensional object space (*x*, *y*, *z*) to two-dimensional detector space (*u*, *v*).

An analytical approach is presented in reference [70]. Two point objects are placed off the rotation axis and on opposite sides of the system's mid-plane (figure 22a). The distance between the two point objects must be known accurately. When the rotation stage performs a complete revolution, each of the point objects ideally traces a circular trajectory in object space (figure 22b). This circular trajectory will be imaged by the detector as an ellipse. Depending on the distance of the point object from the mid-plane, *i.e.* its position in Y, the geometrical properties of the projected ellipse will differ (see figure 25, for example).

The properties of the two ellipses are subsequently used to solve for the geometry of the system, which is defined by a set of seven parameters: *SRD*, *SDD*, θ, φ, η, and principal point. *SDD* is defined in reference [70] as the shortest distance between the source and the detector plane, not necessarily along the magnification axis. The method assumes that the detector has no tilt ($\theta = 0°$); the authors ensured this condition with a level before implementing the procedure. Parameters were evaluated for $N = 6$, 12, and 120 equally-spaced rotation positions over a full revolution of the rotation axis (table 2). The results from different number of rotation positions exhibited only small variations in the estimated parameters, indicating that the method is robust. It is interesting to note that, for the estimation of *SRD* and *SDD*, the values increased with increasing rotation positions; this trend was not observed for the other parameters.
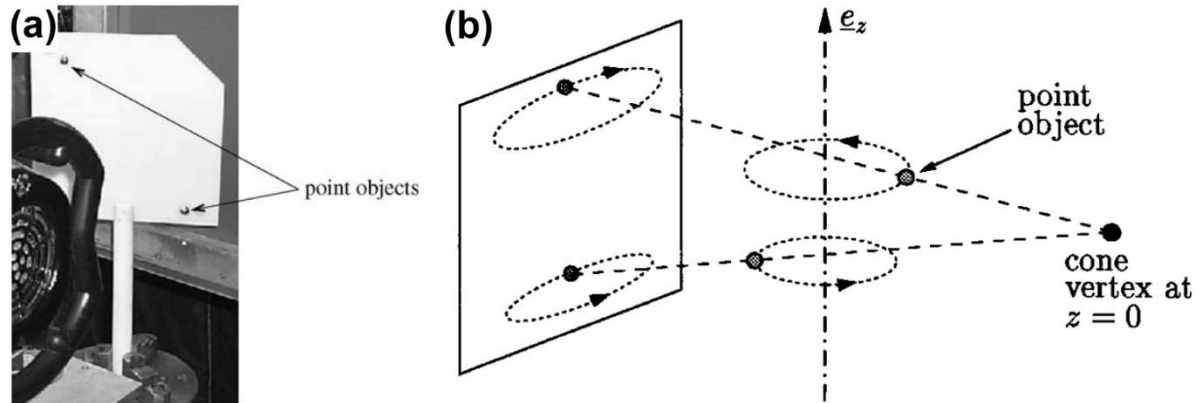
Figure 22. In reference [70] the geometry of the system is defined by a set of seven parameters. (a) The method involves imaging two point objects as they revolve around the rotation axis. (b) The circular trajectories traversed by the point objects in physical space are imaged on the radiograph as ellipses. The authors explain that a series of geometrical analyses can be performed on the imaged ellipses to extract geometrical information about the system [70]. © Institute of Physics and Engineering in Medicine. Reproduced from reference [70] by permission of IOP Publishing. All rights reserved.

Table 2. The authors of reference [70] evaluated the system parameters for $N = 6$, 12, and 120 rotation positions. There were only small deviations in the estimated parameters, indicating a robust method. © Institute of Physics and Engineering in Medicine. Reproduced from reference [70] by permission of IOP Publishing. All rights reserved.

N	SRD (mm)	SDD (mm)	u_o (mm)	v_o (mm)	φ (°)	η (°)
6	377.88	553.49	150.92	202.08	-1.611	-0.304
12	377.90	553.56	151.25	202.08	-1.650	-0.299
120	378.09	553.82	150.88	202.10	-1.607	-0.305

The authors suggest that the accuracy of the parameter estimates strongly depends on the accuracy of locating the centre coordinate of the projected point markers. In order to evaluate the sensitivity of parameter estimation to errors in projection coordinates, the authors apply a 0.1 pixel error to all measured point coordinates. This error corresponds to an error associated with using the centroid function on the projection data to approximate the centre of the point marker. Given the analytical expressions relating each parameter to the set of point coordinates (u_i, v_i), the error in estimated parameters as a result of the coordinate error can be calculated. These error values are presented in table 3. The authors suggest that more than two point objects should be imaged for a complete evaluation of system parameters, *i.e.* $\theta \neq 0°$.

Table 3. Applying a 0.1 pixel error to the measured projection coordinates of each point marker resulted in an error of the various parameter estimates. © Institute of Physics and Engineering in Medicine. Reproduced from reference [70] by permission of IOP Publishing. All rights reserved.

N	ΔSRD (mm)	ΔSDD (mm)	Δu_o (mm)	Δv_o (mm)	$\Delta\varphi$ (°)	$\Delta\eta$ (°)
6	1.093	2.012	2.228	0.497	0.223	0.077
12	1.074	1.936	2.201	0.472	0.221	0.077
120	1.163	2.065	2.133	0.511	0.211	0.083

Studies [71,72] were performed to determine the optimal number and arrangement of point markers. In reference [71], the authors confirmed the suggestion made in reference [70] that a minimum of three point markers is required for providing a unique geometrical solution. It should be noted that this study was performed on a single-photon emission computed tomography (SPECT) system, which has a focal point (pinhole aperture) located between the detector and the axis of rotation. The distance between the point markers should be known *a priori*. The authors observe that the robustness of parameter estimation is strongly dependent on noise in the projections and any errors in the measurement of distance between point markers. A study of covariance uncovered cross correlations in parameters. The authors found that X-offset of translation axis m was highly correlated to u_o, detector tilt θ was highly correlated to v_o, and *SRD* was highly correlated to *SDD*. In-plane rotation of the detector η was the only parameter found to have no clear correlation to other parameters. Detector slant φ was not considered.

In reference [72], the authors use parameter robustness as criteria to determine the optimal configuration of the three point markers. For each configuration, the authors evaluate the variation in estimated parameters as a result of (i) noise in the projection data and (ii) errors in the distances between point markers. The analytical expressions in projection geometry relate the geometrical parameters to the point marker locations (x_i, y_i, z_i) and their projected coordinates (u_i, v_i). The authors use these expressions to calculate the deviation in parameter values as a result of noise in the projected point coordinates and errors in the point marker locations. The standard deviation of parameter estimates from their mean is evaluated. The optimal point marker configuration will exhibit the smallest variation in parameter estimates.

The set of possible point marker configurations is given by a spherical grid, the cross section of which is shown in figure 23a. The authors systematically iterate through the various point marker configurations, each time evaluating the standard deviation of parameter estimates. The authors found two optimal point marker configurations, one which minimized the parameter deviation as a result of noisy projections (figure 23b) and the second minimizing the parameter deviation as a result of errors in the point marker distances (figure 23c). Both optimal setups are shown in the X-Y plane, with the dashed line representing the axis of rotation.
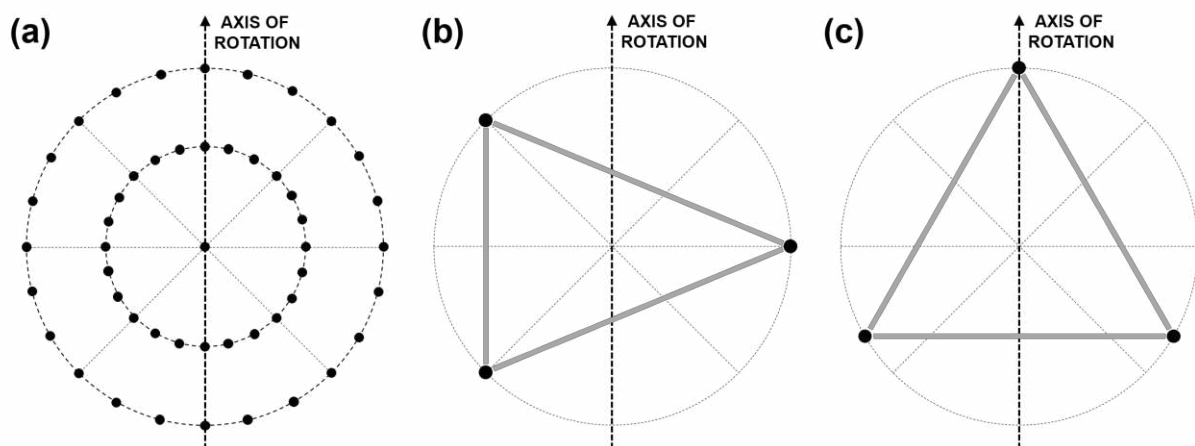

Figure 23. Optimal point marker configurations were investigated in reference [72]. (a) The possible point marker positions were distributed within a spherical grid. Here a cross section of the grid is shown together with the rotation axis. (b) A particular configuration of point markers minimized the effects of noise in the projections. (c) Another configuration minimized the effects of errors in the distances between point markers. © 2005 IEEE. Reprinted, with permission, from reference [72].

In reference [73] the analytical approach seen in reference [70] based on imaging circular trajectories is revisited. In this simulation study, twelve point markers were aligned along a line roughly parallel to the axis of rotation and imaged at 180 positions, *i.e.* 2° angular increments of the rotation axis. Six detector parameters (θ, φ, η, *SDD*, and principal point) were resolved by performing Fourier analysis on the low-frequency components of the elliptical projection coordinates. The method does not require *a priori* spatial information about the point objects; however, *SRD* must be known in advance. The parameters were evaluated for each point marker independently. The averaged parameters were compared to the true values from the model used for simulation. To evaluate the stability of the proposed method, the authors applied Gaussian noise to the simulated projection data. The variance in the twelve sets of estimated parameters is taken as the uncertainty of the averaged parameter estimates. The simulation was performed for various levels of noise, denoted by the standard deviation σ of the Gaussian: 0.01 pixels, 0.1 pixels, 0.2 pixels, and 0.4 pixels. The deviations of each parameter from true value are shown in table 4. While it is clear that the uncertainty in the parameter estimates increases with an increase in the added noise, there is no consistent trend for parameter deviations as a function of added noise.

Table 4. The authors of reference [73] evaluated the robustness of their method by simulating various levels of noise in the projection coordinates of the point markers. Table adapted from reference [73].

Parameter	True value	Gaussian noise with standard deviation σ (pixels)			
		0.01	0.1	0.2	0.4
θ (°)	-1.200	-0.003 ± 0.019	-0.121 ± 0.219	0.225 ± 0.617	-0.083 ± 0.816
φ (°)	1.500	0 ± 0.012	-0.040 ± 0.117	-0.092 ± 0.265	0.137 ± 0.352
η (°)	-1.000	0 ± 4×10⁻⁴	-0.001 ± 0.003	-0.004 ± 0.010	-0.005 ± 0.017
SDD (mm)	701.2	0 ± 0.3	0.4 ± 2.2	-0.4 ± 2.8	-4.3 ± 5.6
u_o (mm)	1.50	0 ± 1×10⁻⁵	0 ± 1.4×10⁻⁴	0 ± 4.2×10⁻⁴	0 ± 6.2×10⁻⁴
v_o (mm)	1.30	0 ± 5×10⁻³	-0.03 ± 0.07	-0.01 ± 0.12	-0.02 ± 0.18

The authors then evaluated the geometry of a test system. As in the simulation study, the geometry is evaluated for each point marker independently and then averaged over the number of point markers. The variance in each parameter is taken to be a measure of uncertainty. The authors note that the uncertainty associated with the estimation of out-of-plane rotations θ and φ is as high as 50 % of the estimated value. A possible reason for this, the authors argue, is the residual distortions in the plane of the detector that result in an erroneous pixel size.

It is interesting to note in table 4 that the uncertainty in estimated out-of-plane rotations increases rapidly with increasing noise in the simulated projections. However, the authors suggest that the effect of out-of-plane rotations to the quality of reconstructed images is small when compared to the same effect caused by an in-plane rotation. The estimated value of *SDD* in both experimental tests is about one half of a centimetre from the reference *SDD*. Erroneous pixel size could also result in this offset of the estimated value. Additionally, the authors argue that the reference *SDD* is difficult to measure accurately as there is some ambiguity as to where the X-ray focal spot is and where the X-rays are absorbed in the detector.

Subsequent to the observations made in reference [73], the analytical method presented in reference [74] assumes that both out-of-plane rotations of the detector are negligible. The authors support this assumption by evaluating the error in projected point coordinates as a result of out-of-plane rotations. It was shown analytically that an out-of-plane rotation of 2° results in a maximum pixel coordinate error of 1 %. In contrast to the method in reference [73], the authors of reference [74] do not require *SRD* to

be known *a priori*; it is acknowledged that there is an ambiguity in the exact measurement of this distance. As a result, the method requires a rough estimate of the distance between two point markers. Thus, the method determines the other five parameters (*SRD*, *SDD*, η, and principal point). An approximately linear set of ball bearings is imaged at multiple rotation positions and the projected elliptical trajectories are analysed. The angular readout of the rotation axis (figure 24a) for each projection is used to identify 'radial pairs', *i.e.* pair of point marker projections separated by a rotation angle of 180° (figure 24b). The distance between projected point markers within each radial pair is calculated.
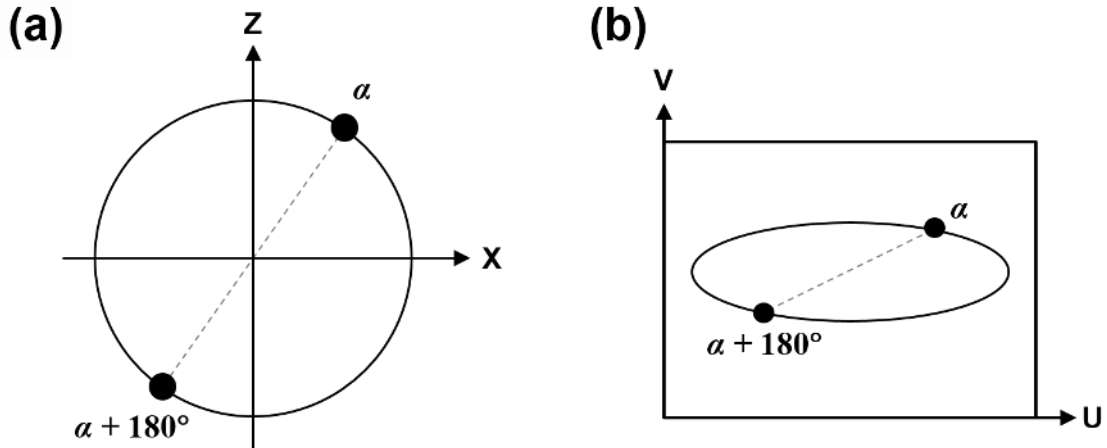

Figure 24. The concept of radial pairs is applied in reference [74]. The distance between two markers in a radial pair on the projected image is greatest when the length segment between the two markers is parallel to the X axis. Alternatively, the shortest distance between two markers in a radial pair on the projected image occurs when the length segment between the two markers is parallel to the Z axis. Figures adapted from reference [74].

The point marker projections that correspond to the radial pairs with the maximum and minimum distances are designated 'benchmark points' and are used for analysis. It should also be noted that the lines connecting point markers within each radial pair intersect at the projected centre of the circular trajectory in object space. The accuracy of the proposed method was evaluated by simulation. The authors applied varying levels of Gaussian noise (σ = 0.1, 0.2, 0.4, and 1.0 pixels) to the centre coordinates of the point projections and observed the resulting deviation in the estimated parameters. Simulations were performed ten times and the standard deviation in parameter estimates was taken to be a measure of uncertainty. This method is applied in reference [75] to provide an initial estimate of the same five parameters. Numerical optimization is then used to solve for detector out-of-plane rotations. In the fitting process, the initial five parameters are also allowed to vary, thus refining their solutions. Table 5 shows the comparison of the results from reference [75] to those from reference [74] with a Gaussian noise of σ = 0.4 pixels on projected point coordinates.

In reference [76], an analytical method is provided to determine the in-plane rotation η independently of θ and φ. The authors exploit the dependence of the projected ellipse to the Y position of the point marker. When the point object is at Y = 0 (on the mid-plane), its trajectory is imaged as a line (figure 25a). The detector in-plane rotation η can be calculated from the slope of this line in the detector coordinate frame. The authors argue that, theoretically, only one point object is required if that point object is exactly positioned on the mid-plane. However, this condition is very difficult to satisfy; therefore, the authors provide a method to determine the slope of this line from a minimum of two objects placed away from the mid-plane. This method is based on principles from perspective geometry,

namely the presence of a converging point in the projection of lines that are parallel in the object space. In particular, the authors circumscribe the circular trajectories with a square, the sides of which are parallel in object space (figure 25b). In the projected ellipse, the parallel sides of the circumscribed square in object space converge to a point (figure 26a-b). Analytical expressions reveal system parameters from the extracted converging point information.

Table 5. The authors of reference [75] propose a method that uses numerical optimization to determine out-of-plane rotations and to refine the parameters that were initially estimated using the method from reference [74]. The results for data with Gaussian noise (σ = 0.4 pixels) is compared to the results from reference [74]. Table adapted from reference [75].

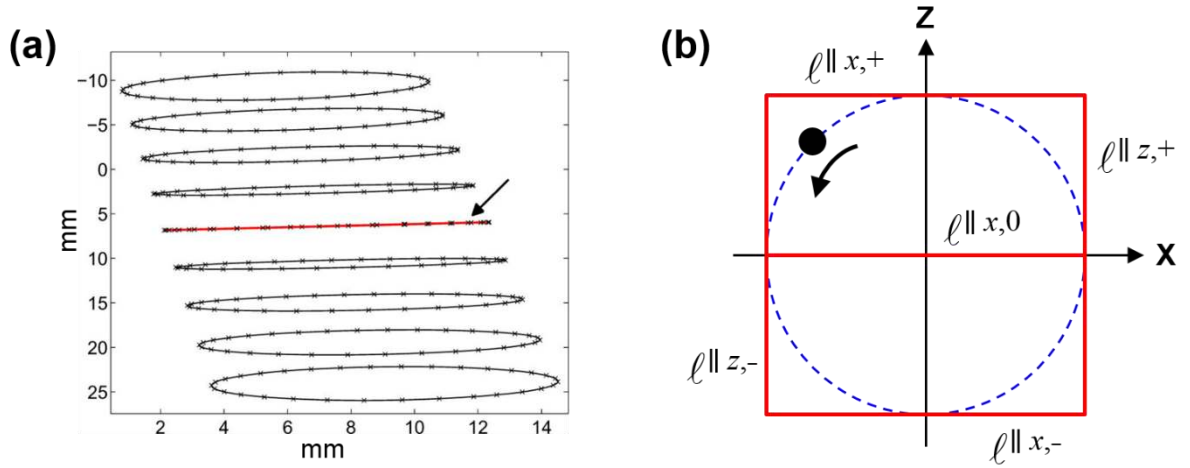| Parameter	True value	Reference [74]	Reference [75]
u_o (pixel)	1005	1005.9±0.3	1005.0±0.0
v_o (pixel)	480	480±1	479.90±0.15
η (°)	-1	-0.99±0.03	-1.0001±0.0002
SRD (mm)	150	150.2±0.5	149.62±0.06
SDD (mm)	400	401±1	399.99±0.06
θ (°)	1.2	Not determined	1.1961±0.0116
φ (°)	1.5	Not determined	1.5018±0.0046

Figure 25. (a) The trajectory of a point marker located on the mid-plane will be imaged as a line. The slope of this line can be used to determine the in-plane rotation η of the detector [76]. The horizontal and vertical axes have units of millimetres. (b) In the absence of a point marker on the mid-plane, two or more point markers located off the mid-plane can be used. The authors first define a set of parallel lines in object space by circumscribing the marker trajectory with a square. Opposing pairs of the square are parallel to each other. © 2012 IEEE. Reprinted, with permission, from reference [76].
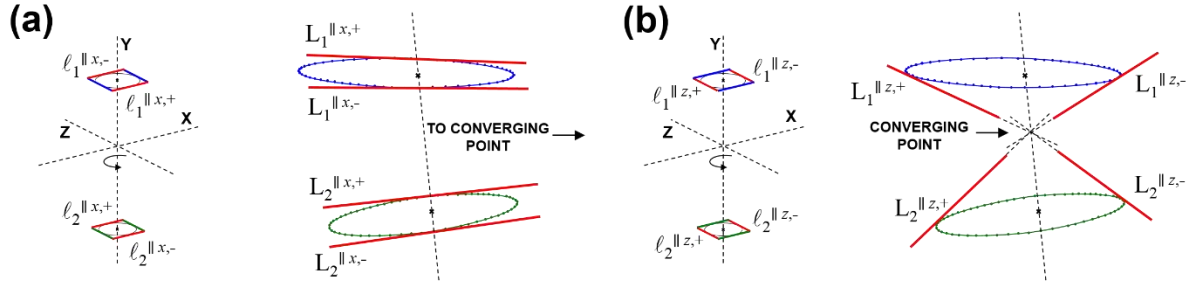
Figure 26. The method proposed in reference [76] exploits a principle from perspective geometry, which states that the projections of parallel lines in object space converge to a point. From the trajectories of two point markers placed on opposite sides of the mid-plane the authors extract two converging points. The converging point in (a) corresponds to the projection of lines parallel to the X axis, while the converging point in (b) corresponds to the projection of lines parallel to the Z axis. © 2012 IEEE. Reprinted, with permission, from reference [76].

By simulating a Gaussian perturbation (σ = 0.1 pixel) of the point projection coordinates, the authors compared the average estimated η from a set of 50 simulations to the true value. The standard deviation of the 50 estimated η values is also calculated. The simulations were repeated for different out-of-plane rotations and the authors confirmed that the quality of the estimated η is independent of the values of θ and φ. It was observed that the standard deviation of the estimated η decreased with increasing rotation positions N.

The method proposed in reference [76] is extended to determine the other six parameters (*SRD*, *SDD*, θ, φ, and principal point) in reference [77]. After determining η, the projection data is rotated to remove the in-plane rotation, which then simplifies the determination of the other six parameters. In both references [76,77] a bias is observed in the parameters estimated from noisy projections. The authors suggest that this bias is most likely a result of errors from the centre determination of finite point markers, as well as systematic errors in the ellipse fitting algorithm. In reference [77] the effect of applying different fitting algorithms is investigated. The authors found that the bias in the estimated parameters varied between fitting algorithms, citing Taubin's ellipse fitting method [78] as the most effective in reducing the observed bias. Any residual bias was observed to depend on the size of the point markers; an increase in point marker size resulted in an increase of bias.

A numerical optimization method was applied to a newly developed bench-top CT system in reference [79]. In particular, the bench-top system allows the mechanical control of the position and orientation of source, rotation stage, and detector (figure 27). It should be noted that the variables used in reference [79] to denote the various translations and rotations are different from the variables used here. In an effort to determine errors in the mechanical movements of the system, the authors image five spherical objects over two hundred equally-spaced rotation positions. For each applied mechanical translation or rotation, the system parameters are fit to the observed projection data. In this study, a model for axis translations and rotations is provided, including parameters for errors in axis scaling and squareness. To evaluate the effectiveness of the method, the authors determined the geometrical parameters for a series of applied movements from a given 'home' geometry of the CT system. For each axis of movement, the authors applied multiple distinct motions. The authors evaluate the average residuals between simulated and observed projections from the numerical optimization procedure for each mechanical movement of the CT system as well as the standard deviations of the residuals. The results suggest that the proposed imaging methods are robust for a variety of system geometries.
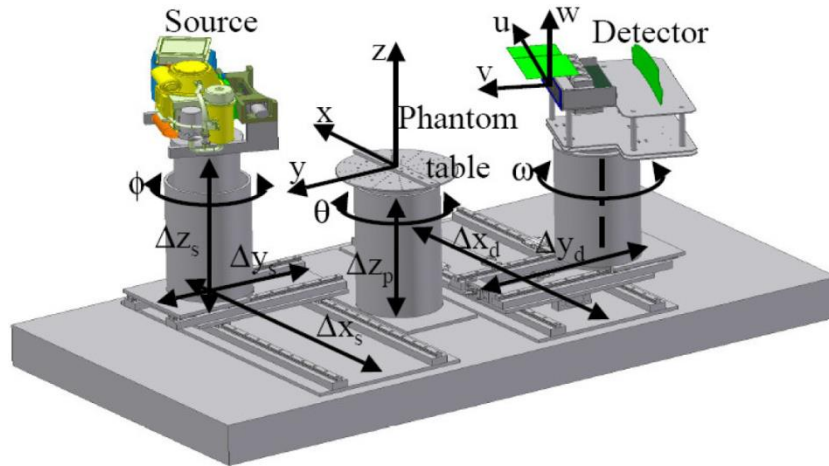
Figure 27. A bench-top CT system allows for the translation and rotation of source, rotation stage, and detector. © 2007 IEEE. Reprinted, with permission, from reference [79].

In reference [80] a cube with twenty-six spheres at known three-dimensional positions is used to solve for *SDD*, θ, η, rotation angle (α), principal point, and source position (in the coordinate frame of the reference object) by way of numerical optimization. A drawback of the cubic object is the high potential for overlap of sphere projections. The same authors subsequently compared the reference object in [80] to a new object in reference [81]. This new object consists of a helical arrangement of spheres (figure 28a). The authors tested the effectiveness of multiple helical arrangements (figure 28b), which differ in the number of spheres and the pitch of the helix; the cubic arrangement from reference [80] was also tested for comparison. The authors applied Gaussian noise ($\sigma = 0.25$ pixels) to 1000 simulated projections of the point markers. The standard deviation of the residuals from numerical optimization on the noisy projections is used as the criterion for determining the effectiveness of the arrangements. The authors found that a helix with higher pitch and more spheres (bottom left of figure 28b) provided the lowest standard deviation. In both references, the detector is compensated for planar distortions prior to performing the parameter evaluation.
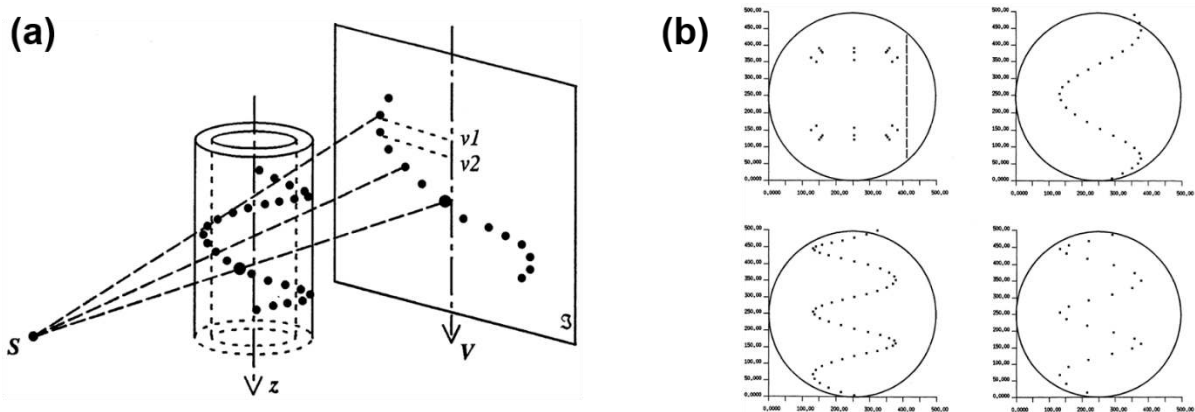

Figure 28. (a) A helical arrangement of point markers is proposed to reduce the occurrence of marker overlap in the projected image. (b) In reference [81] the effectiveness of various helical arrangements was compared to the cubic arrangement (top left) from reference [80]. The standard deviation of residual values from numerical optimization was used as the criterion; the authors found that a helix with more spheres and highest pitch provided the best results (bottom left). Figures from reference [81].

Methods considering rotational error motions

The imaging methods presented up to this point rely on a critical assumption: point objects perform a circular trajectory as they are rotated. This implies that the motion of the rotation axis is perfectly stable. In the presence of rotational instabilities, the methods presented previously could provide erroneous results. In reference [82], numerical optimization was performed on projections of three rotating point markers. After minimization of the cost function, the authors observed systematic residuals between the simulated and observed projections (figure 29a). The authors suggest that the presence of systematic residuals is an indication that the model is not accounting for all behaviours in the test system. Two parameters were subsequently added to model a sinusoidal variation in the detector tilt as a function of rotation angle (figure 29b). These parameters are $\Delta\theta$ and β, which correspond to the amplitude of the tilt oscillation and the phase shift, respectively. Given the new imaging model, the residuals after minimization were reduced (figure 29c). The results indicate that the added terms in the imaging model succeeded in detecting a sinusoidal change in detector tilt as a function of rotation angle.
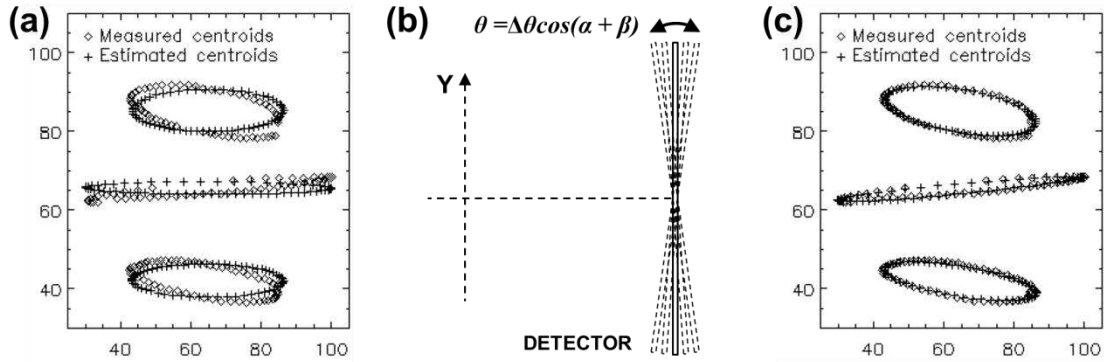

Figure 29. (a) The presence of residual values between simulated and measured point markers projections after numerical minimization is an indication that not all behaviours are considered by the imaging model. (b) The authors adapted their model to consider a sinusoidal variation in detector tilt θ. (c) The optimization procedure was repeated; the residuals decreased as a result of the new tilt parameters. © 2004 IEEE. Reprinted, with permission, from reference [82].

The amplitude of tilt oscillation $\Delta\theta$ was consistently estimated at 0.3°, while the phase shift β was between -0.6° and 0.0°. Table 6 presents the estimated parameters with and without tilt oscillation in the model. It should be noted that this study was performed on a SPECT system. The addition of oscillation amplitude and phase shift in the model resulted in a change of other estimated parameters. For example, estimates of *SDD* and *SRD+SDD* (distance from detector to rotation axis) increased after including tilt oscillation. At the same time, the mechanical offset of the rotation axis m and η were both reduced. The value of u_o shifted from a negative value to a positive value. Changes in the estimates of θ and v_o were not consistently in the same direction. It should be noted that, given a fixed detector, the results in reference [82] are most likely indicative of instabilities in the rotation axis.

The issue of non-ideal rotation is also addressed in reference [83]. The author argues that the parameterization in reference [82] is not adequate to capture small and unpredictable error motions of the geometry. A method is therefore proposed that applies small perturbations to a set of initial parameters, which were estimated assuming ideal rotation. In particular, the perturbations are applied to the parameters that describe the position and orientation of the detector with respect to the rotation axis. These parameters are defined in reference [83] as a translation vector $\mathbf{T} = [t_x, t_y, t_z]$ and the three rotation

angles [θ, φ, η]. The objective of this numerical optimization method is a further reduction of the cost function (between observed and estimated projections of three rotating point markers i = 1, 2, 3) by applying small perturbations to the estimated parameters.

Table 6. The parameters estimated with and without tilt oscillation parameters in the model are compared. The estimation was performed twice for each case. It should be noted that this study was performed on a SPECT system. *SRD* is replaced with *SRD+SDD*, which is the distance from the detector to the rotation axis. The focal point in a SPECT system is located between the detector and the axis of rotation [82]. © 2004 IEEE. Reprinted, with permission, from reference [82].

SDD (mm)	*SDD+SRD* (mm)	*m* (mm)	u_o (mm)	v_o (mm)	θ (°)	$\Delta\theta$ (°)	β (°)	η (°)
Without tilt oscillation								
198.3	241.8	1.4	-6.0	2.3	2.04	0.00	0.00	-0.34
199.8	243.5	0.9	-2.2	-0.6	1.28	0.00	0.00	-0.20
With tilt oscillation								
200.6	244.7	0.2	0.8	3.2	1.11	0.31	-0.09	-0.19
201.6	245.7	0.1	2.3	3.3	1.36	0.31	-0.01	-0.12

To evaluate the effectiveness of their method, the authors applied the concept to simulated data. At each of the 64 equally spaced angular positions (α = 1, 2,…, 64), a pseudo-randomly generated perturbation was applied independently to each translation [t_x, t_y, t_z] and rotation [θ, φ, η] of the detector. The perturbations ranged from 0.5 mm to 3 mm for translations and from 0.5° to 5° for the rotations. Given these perturbations, the exact point projection coordinates for each of the three markers ($u_{i,\alpha}^{exact}$, $v_{i,\alpha}^{exact}$) are calculated. The authors then apply Gaussian noise (σ = 0.2 pixels) to the exact coordinates, yielding a new set of coordinates ($u_{i,\alpha}^{obs}$, $v_{i,\alpha}^{obs}$). These steps are performed on a set of 110 simulated geometries. Given the set of observed point projection coordinates, the authors performed their refined method to estimate the geometrical parameters of the simulated system ($u_{i,\alpha}^{est}$, $v_{i,\alpha}^{est}$). For comparison, the authors also estimate the parameters using the method in reference [71], which assumes ideal rotation. The root-mean-square error between estimated and exact projection coordinates over 110 simulated geometries is calculated for each method using equation (2).

$$\langle E \rangle = \sqrt{\frac{1}{192}\sum_{i=1}^{3}\sum_{\alpha=1}^{64}\left(\left|u_{i,\alpha}^{est}-u_{i,\alpha}^{exact}\right|^2+\left|v_{i,\alpha}^{est}-v_{i,\alpha}^{exact}\right|^2\right)} \qquad (2)$$

Figure 30a presents these errors for each method individually. Each point on the plot corresponds to one of 110 simulated geometries. The points are plotted in order of increasing error for both methods. Figure 30b shows the estimated and observed projections superimposed onto the detector for both the ideal rotation method (left) and the refined method (right).
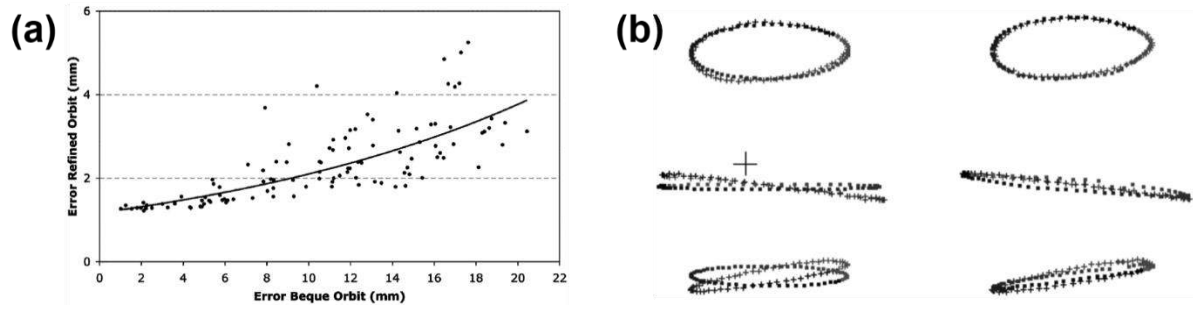
Figure 30. The authors of reference [83] propose a 'refined' method to determine instabilities in the rotation of the stage. The method applies perturbations to the parameters describing the position and orientation of the rotation axis with respect to the gantry. The system parameters are then determined by numerical optimization given a set of noisy ($\sigma = 0.2$ pixels) point projection coordinates. (a) The root-mean-square error between estimated and exact point coordinates is presented for the proposed method and for the method in reference [71], which assumes an ideal rotation. (b) The estimated point projection coordinates for the method assuming ideal rotation (left) and for the refined method (right) are superimposed onto the exact coordinates. © 2008 IEEE. Reprinted, with permission, from reference [83].

The influence of rotational instabilities on the evaluation of system geometry is avoided by the method described in reference [84]. A reference object incorporates a total of twenty-four ball bearings in two circular arrangements within a cylindrical casing (figure 31a). The relative positions between ball bearings must be known accurately. Whereas in references [68–77,79,82,83] the reference objects are imaged at multiple rotation positions and, in some cases, must perform a full revolution, the method in reference [84] allows the geometry of the system to be resolved from one pose. Thus, any instability in the rotation of the stage is of no consequence to the determination of geometrical parameters. The parameters in this study are: source position (x_s, y_s, z_s), detector position (x_d, y_d, z_d), detector rotations (θ, φ, η), principal point, and angle of rotation of the rotation stage (with respect to a chosen datum). The position and rotation parameters are evaluated with respect to a coordinate frame in the reference object. While all other parameters are evaluated analytically, out-of-plane rotations of the detector are estimated by nonlinear root finding (optimization).

The error in the proposed method is evaluated experimentally. Parameter estimation is performed subsequently after accurate offsets are applied to the test system. The newly-measured parameters are then compared to the applied offsets. The error in measuring the displacement in X-ray source was 80 μm in the X and Y directions and 800 μm in the Z direction. On the other hand, the error in detector displacement was 60 μm in X and Y directions. The experimentally observed errors are summarized in table 7.

Table 7. The authors evaluated the effectiveness of their proposed method on a set of accurate displacements of the X-ray source and detector. The error between estimated and applied displacements is presented here. Table based on data from reference [84].

Δx_d (mm)	Δy_d (mm)	Δx_s (mm)	Δy_s (mm)	Δz_s (mm)
0.060	0.060	0.080	0.080	0.800

Another advantage of this method is the ability to characterize non-ideal behaviours of the rotation axis. By measuring source and detector positions as a function of rotation position, the authors were able to observe instabilities in the axis of rotation (see figure 31b). According to the results, the authors observed

precession in the rotation axis of about 0.0115°. This wobble occurred three times within a full revolution of the rotation stage. Error in determining rotation angle was found to be no larger than 0.05°. The rotation angle measurements were compared with the angular encoder readout.
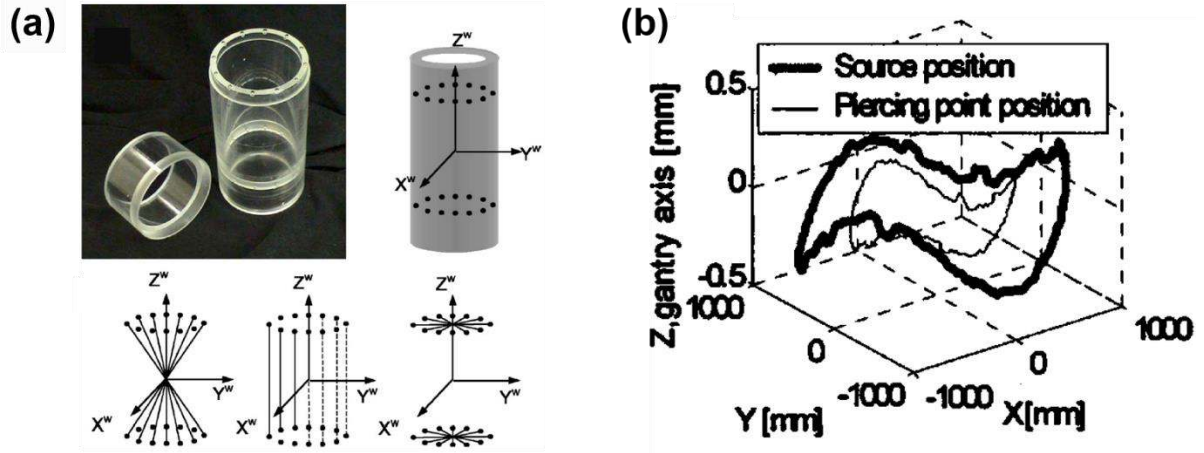

Figure 31. (a) In reference [84], the authors propose a reference object with static circular trajectories, thus removing the need to rotate the object. (b) By evaluating system geometry as a function of rotation angle, the authors in reference [84] observed instabilities of the rotation stage. In this plot, the Z axis corresponds to the rotation axis, while the X axis corresponds to the magnification axis. Figures from reference [84].

The authors argue that the quality of parameter estimation can suffer from uncertainties in the physical position of the markers (fabrication errors) and from uncertainties in the determination of the projected marker centre. Thus, the sensitivity of parameter estimation is evaluated in the presence of 0.1 pixel error in the pixel coordinate of the projected point marker centre. Sensitivity analysis is performed by taking the first derivative of each parameter with respect to the pixel coordinates. Then, given a difference in pixel coordinate of 0.1 pixels, the resultant change in parameter value can be determined. The analysis is repeated for multiple reference objects, each with different numbers of point markers. The authors note that an average reduction of 30% in the change of source position, detector position, and detector angles occurred when the number of point markers increased from 16 to 32. Additionally, the authors evaluate the sensitivity in detector rotations and magnification factor as a function of increasing out-of-plane rotations (figure 32). At $\theta = \varphi = \pm 40°$, the error in rotation angle estimation was less than 0.05° for θ and φ, and 0.005° for η. The error in magnification factor was 0.5 % for the highest out-of-plane rotations.
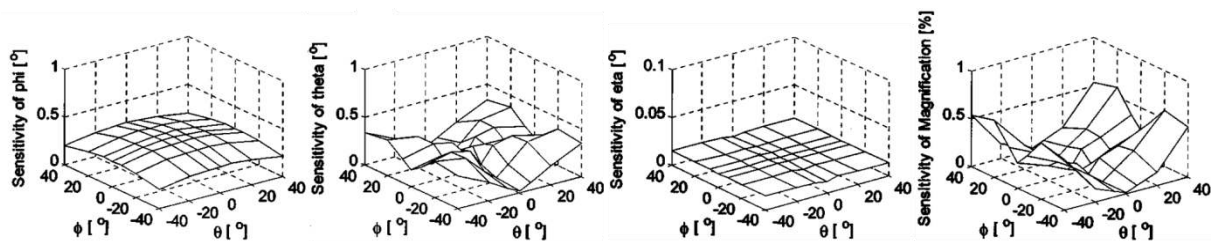

Figure 32. The sensitivity of detector rotations and magnification (due to 0.1 pixel error) was evaluated as a function of out-of-plane rotations. The estimation error of θ and magnification factor increased with increasing out-of-plane rotations. On the other hand, the opposite behaviour is observed for the estimation of φ – the error decreased with increasing out-of-plane rotations. Estimation of η is shown to have little sensitivity to out-of-plane rotations. Figures from reference [84].

The authors suggest that the reference object could also prove useful in determining temporal instabilities (*e.g.* focal spot drift, mechanical vibrations) by observing changes in the system geometry over a given period of time. It should be noted that, since the system geometry evaluated from a coordinate frame fixed to the reference object, some of the observed instabilities as a function of rotation position could be a result of misalignment between the cylindrical axis of the reference object and the axis of rotation. The authors suggest that changing the coordinate frame of the parameter estimates to one that is not fixed to the reference object could resolve this problem. The authors of reference [85] investigate the change in coordinate frame suggested in reference [84]. The authors performed the initial parameter estimation from the coordinate frame of the reference object according to reference [84]. Given the source positions at various rotation angles, the centre of source trajectory (iso-centre) and the orientation of the rotation axis were determined. The authors then evaluate a translation vector $\mathbf{T} = [t_x, t_y, t_z]$ and two rotations (α, β) that describe the transformation from the coordinate frame of the reference object to the new source trajectory frame, which is aligned to the observed axis of rotation and has its origin at the iso-centre. By re-evaluating the parameters in the new frame, the authors suggest that the parameter estimates are no longer influenced by positioning of the reference object.

Indeed, a simulation study [85] confirmed the reduction of the parameter variation when changing coordinate frames. The authors observe that, given the new coordinate frame, the source and detector positions were found to within 100 μm from true. Detector rotations and rotation axis angle were found to within 0.05°, while the principal point was found to within 0.4 pixels. Additionally, the position of the reference object with respect to the iso-centre and its orientation with respect to the rotation axis were found to within 50 μm and 0.1°, respectively.

The advantage of the new coordinate frame is also observed experimentally. The source and detector positions are measured in the reference object coordinate frame and subsequently re-calculated in the iso-centre coordinate frame. Figure 33a shows source and detector trajectories plotted in the object coordinate frame, whereas figure 33b shows the same trajectories in the iso-centre coordinate frame. The apparent tilt of the trajectories in the object frame is removed in the iso-centre frame. However, a closer look at the detector and source trajectories uncovered an offset of the trajectory centres in the X-Z plane (figure 33c). The authors determined that this offset was a result of imprecisions in the point marker positions. To solve this problem, the reference object was rotated by 180° about its cylindrical axis and the parameter estimation is repeated. After averaging the parameters from the two scans, the authors found that the X-Z offset in trajectory centres was greatly reduced (figure 33d). It should be noted that a Y offset remained, for which the authors suggest an additional test.

In other studies, point markers are arranged such that they form orthogonal features. For example, in reference [86] thirteen point markers are aligned along three orthogonal lines with one of the markers serving as a common 'origin' point between the lines. The markers are equally spaced and the distance is known *a priori*. Figure 34a depicts the orthogonal arrangement, albeit with seven point markers. A set of intermediate parameters are calculated from the projected point coordinates; these parameters are then used to determine the geometry of the system by way of analytical expressions. The system is defined by *SDD*, principal point (u_o, v_o), source position (x_s, y_s, z_s), and detector rotations (θ, φ, η) with respect to the axes of the reference object. A scan of the proposed object was simulated to determine the efficacy of their method. The imaging model incorporates a sinusoidal variation of the source and the system parameters were evaluated for each rotation position of the reference object. The authors found that the parameters were estimated to within 0.5 % of true value.
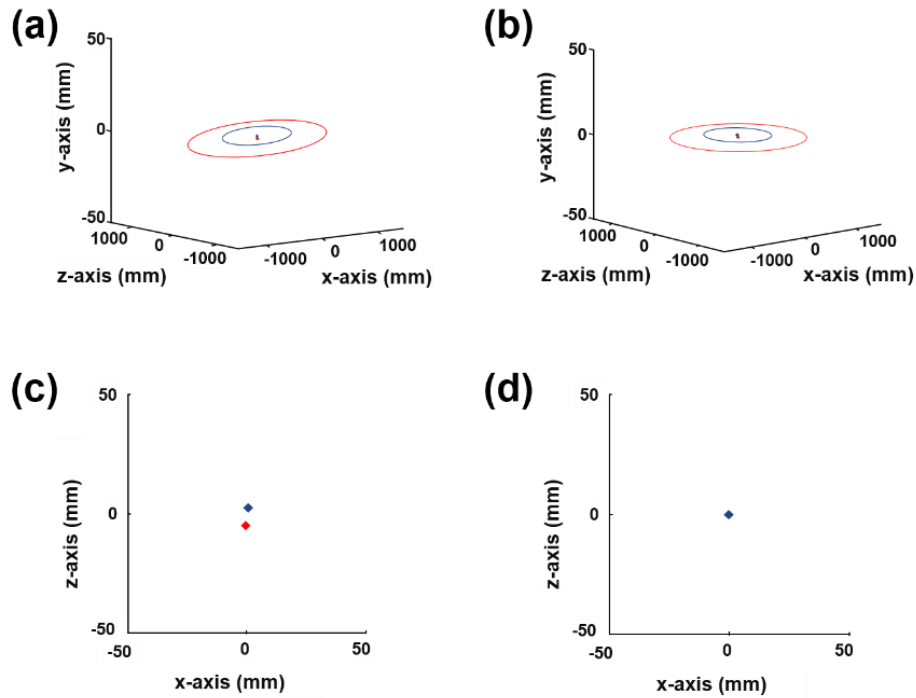
Figure 33. (a) The positions of the source and detector in the reference object coordinate frame are plotted as functions of rotation angle. A tilt in the trajectories is visible. (b) Once the positions were re-calculated in the iso-centre coordinate frame, the tilt is removed. (c) Upon closer inspection along the X-Z plane, an offset between the centre of source trajectory and the centre of detector trajectory was observed. (d) The test scan was repeated with a rotated orientation of the reference object (180° about cylindrical axis). Averaging each estimated trajectory over the two scans removed the offset in the X-Z plane. Figures from reference [85].

A slightly modified reference object was presented in a subsequent study [87]. A total of six markers are arranged to form three orthogonal lines without a common marker at their intersection. The method requires the reference object to be positioned such that three of the markers are above the mid-plane while the other three are below. In particular, the triangles traced by each set of three markers should ideally be parallel to the mid-plane. This arrangement reduces the chance of overlap between imaged markers, which can have detrimental effects to the quality of parameter estimation. The authors suggest that decreasing the size of the markers and increasing their spacing can also reduce likeliness of overlap. Simulations were performed on the proposed reference object: one assumed a circular trajectory of the X-ray source (stable rotation) while the other allowed for small and random perturbations of the geometry. Additionally, the simulations assumed that the reference object was not perfectly aligned. In both cases, the authors evaluated the accuracy of the parameter estimates. *SDD* and principal point were estimated to within 1 mm. Source position was found to be within 0.5 mm along the X and Z directions and within 0.1 mm along the Y direction. Out-of-plane rotations of the detector were within 0.1°, while in-plane rotation was estimated to within 0.02° from true. In the case of large deviations in the rotation axis, there is an increased possibility of overlap between imaged balls. The authors of reference [88] therefore suggest incorporating two additional spheres oriented diagonally (in addition to twelve spheres along three orthogonal lines) to compensate for any overlapping that may occur. In this study, the estimated detector and source positions were also found to within 0.5 mm. Detector out-of-plane rotation angles were estimated to within 0.05°, while the in-plane rotation was also found to within 0.02°. The authors noticed a bias in their estimated *SRD* and *SDD* of 0.1 mm; this is believed to be a result of using centroids to define the centre projections of point markers. The topic of identifying the projection of the sphere centre is discussed in more detail in other publications [89–91].
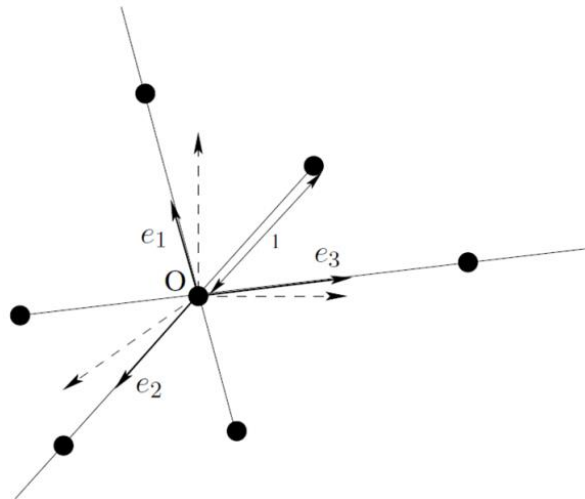
Figure 34. Point markers are arranged such that the lines connecting each set of three form an orthogonal set. © 2005 IEEE. Reprinted, with permission, from reference [86].

5.2 METHODS BASED ON REFERENCE INSTRUMENTS

Several studies have been conducted to directly measure errors in the kinematic assembly of XCT systems. These studies are based on the use of reference instruments to perform measurements. For example, one study [32] investigated the errors in positioning of the rotation stage along the Z-axis. A reference rotation stage position was chosen and the distance to subsequent positions (spaced 50 mm apart) was measured with an interferometer. The authors compared the interferometer measurements to the readout of the system's linear encoder. Measurements were performed for a total travelling range of 700 mm and for both rotation stage travelling directions. The results are shown in figure 35. As the Z position increases, the rotation stage approaches the detector and the magnification decreases.
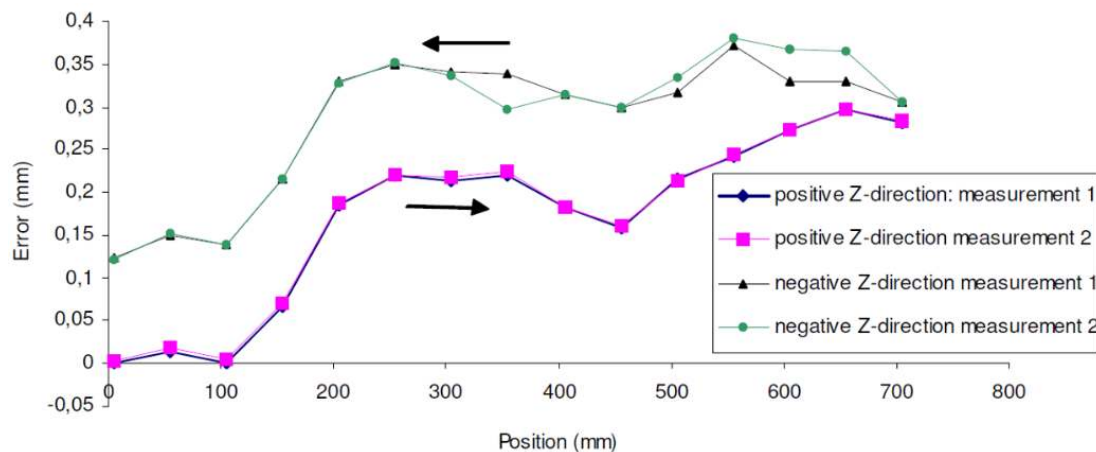

Figure 35. Positioning errors were observed for translation of the rotation stage along the magnification axis. The errors were measured for both directions of movement. The test was performed twice and the results are shown to be repeatable, indicating a systematic trend. Figure from reference [32].

The error in Z-axis positioning followed similar trends for both directions of travel. In general, the errors increased with increasing Z position. The tests were repeated and results show that the positioning along the positive direction is more repeatable (at further positions) than the positioning along the negative

35

direction. It is interesting to note the magnitude of the errors. The errors along the positive Z direction were nearly 300 μm at a distance of 650 mm. Errors along the negative Z direction were even higher – nearly 400 μm at a distance of 550 mm. Thus, the plot shows that the largest positioning errors occur at low magnification. An error in the Z position of the rotation stage results in an error in the registered *SRD* and, subsequently, an error in the magnification factor applied to the detector pixels. The simulation in reference [35] showed that measurement error was less sensitive to object positioning errors at low magnification positions. This sensitivity is evident given the inverse relationship between magnification and *SRD*. The first derivative of the magnification equation with respect to *SRD*,

$$\frac{dM}{d(SRD)} = \frac{d}{d(SRD)}\left(\frac{SDD}{SRD}\right) = \frac{-SDD}{SRD^2} \tag{3}$$

indicates that an error in *SRD* at lower *SRD* values (higher magnification) will result in a larger error in *M* than the same error at higher *SRD* values (lower magnification). The positioning errors along the negative axis direction are on the order of 100 μm at high magnification.

Another study investigated geometrical errors in the kinematic assembly of a 450 kV XCT system [63]. In this study, the authors developed an error model to estimate how errors in positioning, straightness, and angular motion of the translation axes would affect XCT measurements. Each error parameter was determined by way of reference instruments; in this case, a laser interferometer and an electronic level. Some of the results are shown in figure 36; in particular, the plots represent those error motions that would result in an error of the magnification of the rotation axis. Figure 36a presents Z axis positioning errors as a function of distance from a datum position. The authors observed an error in Z positioning of up to 400 μm along each direction of travel (300 mm on each side). This corresponds to a total positioning error of 800 μm over a traveling distance of 600 mm. Figure 36b shows the measured straightness error of the Y axis along the Z direction. The results indicate that the rotation stage experiences motion in Z of up to about 40 μm in a traveling distance of 200 mm along the Y axis; this error motion in Z occurs between Y ≈ 350 mm and Y ≈ 550 mm. The implications of this error motion are the same as for positioning errors: an error in the registered magnification of the rotation axis. Figure 36c is a plot of the angular error motion of the rotation stage about the X axis as it moves along the Z axis. The authors observed an angular error motion of up to 0.5 mm/m (0.0286°) along each direction of travel (300 mm on each side). This corresponds to a total error motion of 1 mm/m (0.0572°) over a traveling distance of 600 mm. This angular error motion translates to a tilt of the rotation axis. In the case that the rotation axis is not perpendicular to the magnification axis, the rotation axis will occupy multiple magnification positions.
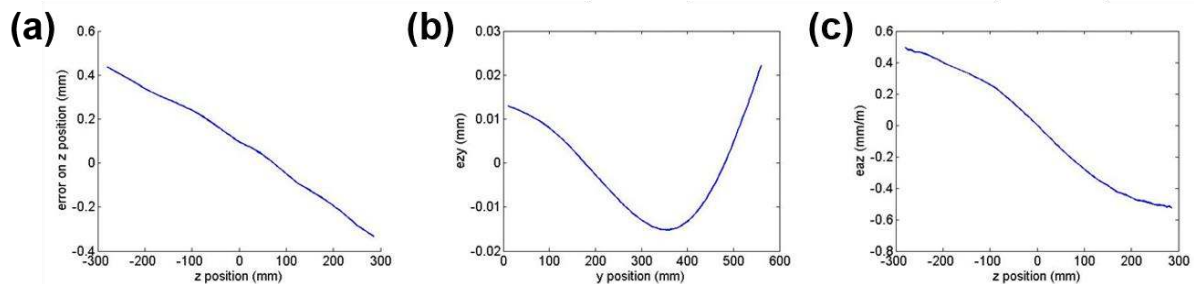

Figure 36. Several error motions will result in an erroneous magnification of the rotation axis: (a) positioning errors of the Z axis, (b) straightness errors of Y axis along Z, and (c) tilt error motion of Z axis about the X axis. Figures from reference [63].

The measured values were applied to the error model and a simulation was performed to estimate measurement errors on a calibrated object. Simulated errors are compared to the errors observed in an actual XCT measurement of the calibrated object. The calibrated object consists of ruby spheres of various diameters mounted on carbon fibre rods and placed on a circular terraced platform (figure 37a). The features to be measured on the object are the distances between sphere centres, sphere diameters, and form.

Measurements were performed at various magnification positions of the XCT system. The experimentally-determined sphere distance errors are plotted as a function of calibrated sphere distance in figure 37b. Errors as simulated by the kinematic error model are also plotted. In order to take into account the uncertainty in the determination of kinematic error parameters, the authors repeated the simulation thirty times. Each time a simulation was run, the input parameters were changed by an amount that was representative of the uncertainty interval associated with their reference measurement. The upper and lower limits of simulated measurement errors are said to represent the 95 % uncertainty interval and are shown in the plot. Figure 37b confirms the agreement between the simulated and observed ('real') measurement errors.
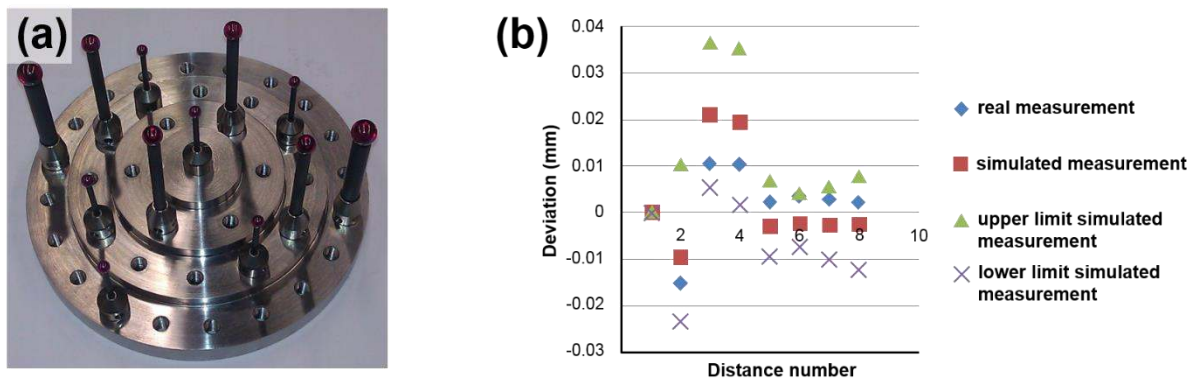

Figure 37. The effects of kinematic errors on the measurement of a calibrated object were studied. (a) The object consists of a collection of ruby spheres. (b) Observed measurement errors were compared to simulated errors based on an error model, the parameters of which were directly determined on the test system. Figures from reference [63].

6   SUMMARY AND CONCLUSION

X-ray computed tomography is seen as a potentially effective tool for dimensional inspection of complex parts. In particular, XCT provides users with the ability to measure internal features otherwise inaccessible by conventional coordinate measuring systems. While the technology is available and the benefits are known, the methods to establish measurement assurance for XCT systems are lacking. In this paper a review of the research efforts that contribute to the development of a geometrical calibration procedure for XCT systems is provided. The geometrical construction of an industrial cone-beam XCT system was described and the various offsets and misalignments that affect the quality of measurements (geometrical influence factors) were outlined. The application of measurement models to simulation studies is discussed. Then, methods to estimate geometrical errors are presented. First, imaging methods, which are based on the imaging of reference objects, are presented. These imaging methods are ideal for evaluating fixed imaging geometries. Industrial XCT systems are often equipped with a kinematic positioning system, which allows users to translate the rotation stage in the measurement volume. The

research on determination of kinematic error motions, which is based on the use of reference instruments, is also presented.

The role of measurement models is critical in understanding how geometrical errors affect the quality of measurements. In particular, models allow the parameterization of each geometrical error, which is useful for evaluating sensitivity coefficients. In this way, geometrical errors that have a critical impact on measurements can be prioritized in any future calibration procedure. It was shown through simulation in reference [35] that errors in Z-axis position of X-ray source and rotation axis have a greater effect on length measurement errors than errors in the Z-axis position of the detector. It was also observed that measurement errors as a result of Z-axis position errors did not have a strong dependence on the position of the projected object in the detector plane. This is expected, as an error in the Z position of the rotation axis results in an error of the magnification factor, which is a global scaling error. Additionally, the authors of reference [35] found that out-of-plane rotations θ and φ of 10° resulted in errors up to 1.5 % of the measured length, while an in-plane rotation η of 0.4° resulted in errors up to 0.1 % of the measured length at high magnifications. It was also observed that measurement errors due to η increased with increasing distance from the detector centre. The authors of reference [35] argued that in-plane rotations are easily compensated in the software, thus limiting the maximum simulated in-plane rotation. Another simulation study found that an X offset of the rotation axis m of 700 μm (corresponding to a shift of two pixels on the simulated detector) resulted in an error of about 2.5 % of measured length.

Additionally, measurement models can be applied 'inversely' for the development of experimental test procedures to map the geometry of an actual measuring instrument. In this review, this principle was observed in section 5.1 on imaging methods. The literature from the industrial XCT community [6,50–55] indicates that current practice only considers global scaling errors in the measurement. Certain geometrical influence factors result in non-uniform errors (as shown in reference [56]) as well as reconstruction errors; therefore, global scale error compensation is not exhaustive. Other imaging methods were developed to determine geometrical influence factors. A hole plate was applied to determine alignment parameters through a series of measurement procedures in reference [65]. Several methods to determine detector distortions were presented in references [61,62]. In reference [59], the drift of the focal spot was observed. Also, tilts of the axis of rotation about the X axis were measured in references [63,64].

A particular group of imaging methods (overwhelmingly from the field of medical physics) are based on reference objects consisting of point markers [66,68–77,79–81]. Some imaging methods evaluated the system geometry by directly solving analytical expressions, while other methods iteratively solved for geometrical parameters by fitting simulated projections to a set of experimentally acquired projections. More recent imaging methods [82–88] have been designed to account for instabilities of the rotation axis, such as tilt error motion or positional drifts. However, a disadvantage of imaging methods is that they are only applicable for fixed kinematic configurations of the rotation stage. Thus, imaging methods would have to be performed every time the position of the rotation stage is changed. The authors of imaging studies consistently found that the accuracy of parameter estimation strongly depended on the ability to accurately locate point projection coordinates in the radiographs. In fact, correct identification of the centres of point objects from their projections is a topic of other research [89–91]. Also, it is shown in reference [85] that imaging methods can suffer from non-ideal placement of the reference object, as well as imprecisions in the measured point marker positions within the object. The parameters evaluated by the various imaging methods are presented in table 8, together with the references in which they are measured.

Table 8. In the table below, the geometrical parameters are listed along with the references, in which the parameters are determined. Additionally, a short description on the influence of each parameter to the measurement volume is provided.

Parameter	References	Influence on measurements
SRD	[57-60[a],65,66[b],68-70,71-72[c],74,75,77,79,80-81[d], 82[c],84-88[d]]	An error in SRD results in a scaling error of the measurement volume. The sensitivity to SRD increases with magnification.
SDD	[57-60[a],66[b],68-70,71-72[c],73-75,77,79-81[e], 82[c],83-85[e], 86-88]	An error in SDD results in a scaling error of the measurement volume.
u_o	[65-66,68-75,77,79-81[f],82,83[f],84-88]	Deviations in the principal point from the detector centre can result in reconstruction errors unless the reconstruction software can accommodate such deviations.
v_o	[65-66, 68-75,77,79-81[f],82,83[f],84-88]	
θ	[66,70-73,75,77,79-88]	Detector tilt and slant will result in form errors due to changes in aspect ratio of similar objects at different regions of the detector.
φ	[66,70,73,75,77,79-81,83-88]	
η	[65-66,70-77,79-88]	Detector skew can result in reconstruction errors unless the reconstruction software can accommodate a tilted rotation axis.
m	[65,66[b],68,71-72,82]	A horizontal (X) offset of the rotation axis can result in reconstruction errors unless the reconstruction software can accommodate a non-central rotation axis.
θ_r	[63,64,66[b]]	A tilt of the rotation axis about the X axis will result in the object being magnified differently along the rotation axis.
α	[84,85]	An error in the angular readout can result in reconstruction errors since the angle position is one of the reconstruction algorithm inputs.

Detector distortions	[61,62]	Distortions in the plane of the detector will result in reconstruction errors as the attenuation paths will be incorrectly backprojected.

[a] In references [57-60] the drift in X-ray focal spot is observed.

[b] The author of reference [66] defines all parameters as deviations in the detector position and orientation.

[c] In references [71,72,82], the studies are performed on SPECT systems, in which the focal point (pinhole aperture) is located between the detector and the axis of rotation.

[d] In reference [80-81,84-88], SRD is given by the position of the X-ray source with respect to the reference object coordinate frame.

[e] In references [79-81,83-85], the position of the detector is defined as the position of the detector in the reference object coordinate frame.

[f] In references [79-81,83], the principal point was defined as a three-dimensional coordinate position with respect to reference object frame.

The kinematic axes are critical to users who want to measure objects of varying sizes. It has been shown that kinematic error motions, such as positioning errors, lack of squareness between axes, straightness errors, and rotational errors (roll, pitch, and yaw) can be measured. For example, experimental studies in references [32,63] found their system to have positioning errors of the Z axis of up to 800 μm for a total axis displacement of 600 mm. Additionally, the same Z axis displacement exhibited a tilt error about the X axis (resulting in a tilt of the rotation axis θ_r) of almost 0.06°. Straightness errors of the Y axis up to about 40 μm along the Z direction were observed for a traveling distance of 200 mm. One of the issues with the methods used to determine kinematic error motions is the requirement for reference instruments. In this case, high-precision instruments such as laser interferometers were used. While these instruments are common place in research laboratories, they may not be practical for all users of XCT.

In order to achieve the goal of establishing traceability of measurements made on XCT systems, it is important that users are equipped with the knowledge to evaluate the necessary measurement uncertainty. Typically, measurement uncertainty can be assessed through a systematic evaluation of all influence factors in a measurement procedure. Methods to determine geometrical influence factors, *i.e.* influence factors particularly related to the system geometry, have been presented in this review. However, these methods are limited in their practical application by users of XCT systems. Determination of mechanical error motions of the kinematic axes requires the use of expensive reference instruments, the operators of which require training. On the other hand, imaging methods can be an easier and cheaper solution since their application only requires the imaging of a reference object. However, a drawback of imaging methods is that they can only be applied to determine the system geometry for a single position of the rotation stage. Imaging methods in their current state require a significant amount of image processing. Additionally, compensation of reconstruction errors from geometrical offsets and tilts, *i.e.* errors that cannot be compensated by applying corrections to the radiographic or voxel data, require access to the reconstruction algorithm; many users of commercial XCT systems do not have this access.

Future research should be dedicated to the development of methods that are practical for users of XCT systems. Such methods should not be time consuming, nor should they require the use of expensive equipment. A possible solution includes the use of reference objects, which is in line with the imaging methods presented in this review. Ideally, this solution would also consider error motions of the

kinematic axes without the need for a separate setup. Such a method would allow the user to map the errors in their measurement volume for consideration into measurement compensation. In addition to evaluating the geometrical parameters, the user would benefit from the assessment of uncertainty in the measured geometrical parameters. As there can be instances in which users cannot access the reconstruction algorithm, a guideline for assessing measurement uncertainty as a result of the non-adjustable geometrical errors should be developed.

The first step in designing effective geometrical calibration and correction methods involves determining the sensitivity of measurements to each geometrical parameters. In some cases, there could be correlation between various parameters; mathematical models and simulation can be useful tools in decoupling the effects of various parameters. The sensitivity analysis will inform the development of geometrical calibration procedures by identifying the critical parameters to be measured in the system. The next step is to design suitable reference objects and test procedures to allow users to measure the geometry of their system. To ensure metrological traceability of the geometrical calibration results, the reference object should incorporate one or more calibrated features, such as the distance between sphere centres. Also, the procedure should provide guidelines for propagating uncertainty in the calibrated features to uncertainty in the measured geometry. Similarly, the uncertainty associated with applying corrections should also be evaluated. Finally, suggestions for incorporating the uncertainty in both procedures to the final measurement uncertainty should be given.

ACKNOWLEDGEMENTS

REFERENCES

[1]   Kruth J P, Bartscher M, Carmignato S, Schmitt R, De Chiffre L and Weckenmann A 2011 Computed tomography for dimensional metrology *CIRP Ann. - Manuf. Technol.* **60** 821–42

[2]   De Chiffre L, Carmignato S, Kruth J-P, Schmitt R and Weckenmann a. 2014 Industrial applications of computed tomography *CIRP Ann. - Manuf. Technol.* **63** 655–77

[3]   Müller P, Hiller J, Dai Y, Andreasen J L, Hansen H N and De Chiffre L 2014 Estimation of measurement uncertainties in X-ray computed tomography metrology using the substitution method *CIRP J. Manuf. Sci. Technol.* **7** 222–32

[4]   Hsieh J 2009 *Computed tomography: Principles, design, artifacts, and recent advances* (Bellingham: SPIE Press)

[5]   Buzug T M 2008 *Computed tomography: From photon statistics to modern cone-beam CT* (Berlin: Springer-Verlag)

[6]   Müller P 2012 *Coordinate metrology by traceable computed tomography* (PhD Thesis, Technical University of Denmark)

[7] Carmignato S, Pierobon A, Rampazzo P, Parisatto M and Savio E 2012 CT for industrial metrology – accuracy and structural resolution of CT dimensional measurements *Conference on Industrial Computed Tomography (ICT)* (Wels, Austria) pp 161–72

[8] Angel J and De Chiffre L 2014 Comparison on computed tomography using industrial items *CIRP Ann. - Manuf. Technol.* 4–7

[9] VDI/VDE 2630-1.2 2010 Computed tomography in dimensional measurement - Influencing variables on measurement results and recommendations for computed-tomography dimensional measurements (Duesseldorf: VDI/VDE Society for Metrology and Automation Engineering)

[10] Bartscher M, Hilpert U, Goebbels J and Weidemann G 2007 Enhancement and proof of accuracy of industrial computed tomography (CT) measurements *CIRP Ann. - Manuf. Technol.* **56** 495–8

[11] Christoph R and Neumann H J 2012 *X-ray tomography in industrial metrology* (Munich: Suddeutscher Verlag onpact GmbH)

[12] Weckenmann A and Krämer P 2010 Computed tomography for application in manufacturing metrology *Key Eng. Mater.* **437** 73–8

[13] Hartley R and Zisserman A 2003 *Multiple view geometry in computer vision* (Cambridge, UK: Cambridge University Press)

[14] ANSI/ASME B5.54 2005 Methods for performance evaluation of computer numerically controlled machining centers (New York: The American Society of Mechanical Engineers)

[15] Furutani R, Shimojima K and Takamasu K 2003 Kinematical calibration of articulated CMM using multiple simple artifacts *Proceedings, XVII IMEKO World Congress* (Dubrovnik, Croatia) pp 1798–801

[16] Sartori S and Zhang G X 1995 Geometric error measurement and compensation of machines *CIRP Ann. - Manuf. Technol.* **44** 599–609

[17] Abbe M, Takamasu K and Ozono S 2011 Calibration of CMM by 3-dimensional coordinate comparison *Proceedings of ASPE 16th Annual Meeting* (Crystal City, USA) pp 2–5

[18] Arriba L, Trapet E, Bartscher M, Franke M and Balsamo A 1999 Methods and artifacts to calibrate large CMMs *Proceedings of the 1st International EUSPEN Conference* (Bremen, Germany)

[19] Balsamo A, Di Ciommo M, Mugno R and Sartori S 1996 Towards instrument-oriented calibration of CMMs *CIRP Ann. - Manuf. Technol.* **45** 479–82

[20] Busch K, Kunzmann H and Wildele F 1985 Calibration of coordinate measuring machines *Precis. Eng.* **7** 139–44

[21]   Schwenke H, Knapp W, Haitjema H, Weckenmann A, Schmitt R and Delbressine F 2008 Geometric error measurement and compensation of machines—An update *CIRP Ann. - Manuf. Technol.* **57** 660–75

[22]   Flack D 2011 *Good Practice Guide No. 42 - CMM Verification* (Teddington: National Physical Laboratory)

[23]   ISO 10360-3 2001 Geometrical Products Specifications (GPS) — Acceptance and reverification tests for coordinate measuring machines (CMM) Part 3: CMMs with the axis of a rotary table as the fourth axis (Geneva: International Organization for Standardization)

[24]   Hu C, Zhu Y, Hu J, Xu D and Zhang M 2013 An on-axis self-calibration approach for precision rotary metrology stages based on an angular artifact plate *Meas. Sci. Technol.* **24** 085007 http://dx.doi.org/10.1088/0957–0233/24/8/08

[25]   Park S-R, Hoang T-K and Yang S-H 2010 A new optical measurement system for determining the geometrical errors of rotary axis of a 5-axis miniaturized machine tool *J. Mech. Sci. Technol.* **24** 175–9

[26]   ISO 230-7 2006 Test code for machine tools — Part 7: Geometric accuracy of axes of rotation (Geneva: International Organization for Standardization)

[27]   Hiller J, Maisl M and Reindl L M 2012 Physical characterization and performance evaluation of an x-ray micro-computed tomography system for dimensional metrology applications *Meas. Sci. Technol.* **23** 085404 http://dx.doi.org/10.1088/0957–0233/23/8/08

[28]   Quarteroni A 2009 Mathematical models in science and engineering *Not. AMS* **56** 10–9

[29]   Cox M G, Forbes A B, Harris P M and Peggs G N 1998 *Determining CMM behaviour from measurements of standard artefacts* (Teddington: National Physical Laboratory)

[30]   Muralikrishnan B, Sawyer D, Blackburn C, Phillips S, Borchardt B and Estler W T 2009 ASME B89.4.19 Performance evaluation tests and geometric misalignments in laser trackers *J. Res. Natl. Inst. Stand. Technol.* **114** 21–35

[31]   Muralikrishnan B, Ferrucci M, Sawyer D, Gerner G, Lee V, Blackburn C, Phillips S, Petrov P, Yakovlev Y, Astrelin A, Milligan S and Palmateer J 2013 Volumetric performance evaluation of a laser scanner *Proceedings of ASPE 28th Annual Meeting*

[32]   Welkenhuyzen F, Kiekens K, Pierlet M, Dewulf W, Bleys P, Kruth J-P and Voet A 2009 Industrial computer tomography for dimensional metrology: Overview of influence factors and improvement strategies *4th International Conference on Optical Measurement Techniques* vol 100 (Antwerp, Belgium) pp 401–10

[33]   BIPM, IEC, IFCC, ILAC, ISO, IUPAC, IUPAP and OIML JCGM 100 2008 Evaluation of measurement data — Guide to the expression of uncertainty in measurement (Geneva: International Organization for Standardization)

[34]   Cox M G and Siebert B R L 2006 The use of a Monte Carlo method for evaluating uncertainty and expanded uncertainty *Metrologia* **43** S178–88

[35]   Kumar J, Attridge A, Wood P K C and Williams M A 2011 Analysis of the effect of cone-beam geometry and test object configuration on the measurement accuracy of a computed tomography scanner used for dimensional measurement *Meas. Sci. Technol.* **22** 035105 http://dx.doi.org/10.1088/0957–0233/22/3/03

[36]   Wenig P and Kasperl S 2006 Examination of the measurement uncertainty on dimensional measurements by X-ray computed tomography *European Conference on Non-Destructive Testing* (Berlin, Germany)

[37]   EN 16016-4 2011 Non destructive testing — Radiation methods — Computed tomography Part 4 : Qualification (Brussels: European Committee for Standardization)

[38]   Holt K M 2007 Geometric calibration of third-generation computed tomography scanners from scans of unknown objects using complementary rays *IEEE Int. Conf. Image Process.* **4** 129–32

[39]   Panetta D, Belcari N, Del Guerra A and Moehrs S 2008 An optimization-based method for geometrical calibration in cone-beam CT without dedicated phantoms *Phys. Med. Biol.* **53** 3841–61

[40]   Kyriakou Y, Lapp R M, Hillebrand L, Ertel D and Kalender W A 2008 Simultaneous misalignment correction for approximate circular cone-beam computed tomography *Phys. Med. Biol.* **53** 6267–89

[41]   Patel V, Chityala R N, Hoffmann K R, Ionita C N, Bednarek D R and Rudin S 2009 Self-calibration of a cone-beam micro-CT system *Med. Phys.* **36** 48–58

[42]   Kingston A, Sakellariou A, Varslot T, Myers G and Sheppard A 2011 Reliable automatic alignment of tomographic projection data by passive auto-focus *Med. Phys.* **38** 4934–45

[43]   Bronnikov A V 2011 A new algorithm for geometric self-calibration in cone-beam CT *Proceedings of the 11th International Meeting on Fully Three-Dimensional Image Reconstruction in Radiology and Nuclear Medicine* (Potsdam, Germany) pp 175–8

[44]   Wein W, Ladikos A and Baumgartner A 2011 Self-calibration of geometric and radiometric parameters for cone-beam computed tomography *Proceedings of the 11th International Meeting on Fully Three-Dimensional Image Reconstruction in Radiology and Nuclear Medicine* (Potsdam, Germany) pp 1–4

[45]   Tan S, Cong P, Liu X and Wu Z 2013 An interval subdividing based method for geometric calibration of cone-beam CT *NDT E Int.* **58** 49–55

[46]   Meng Y, Gong H and Yang X 2013 Online geometric calibration of cone-beam computed tomography for arbitrary imaging objects *IEEE Trans. Med. Imaging* **32** 278–88

[47]   Tekaya I Ben, Kaftandjian V, Buyens F, Sevestre S and Legoupil S 2013 Registration-based geometric calibration of industrial X-ray tomography system *IEEE Trans. Nucl. Sci.* **60** 3937–44

[48]   Muders J and Hesser J 2014 Stable and robust geometric self-calibration for cone-beam CT using mutual information *IEEE Trans. Nucl. Sci.* **61** 202–17

[49]   Zhang F, Du J, Jiang H, Li L, Guan M and Yan B 2014 Iterative geometric calibration in circular cone-beam computed tomography *Opt. - Int. J. Light Electron Opt.* **125** 2509–14

[50]   Bartscher M and Wäldele F 2004 Computed Tomography – a highly potential tool for industrial quality control and production near measurements *8th International Symposium on Measurement and Quality Control in Production* (Erlangen, Germany) pp 3–8

[51]   Kasperl S, Hiller J and Krumm M 2009 Computed tomography metrology in industrial research & development *Materialprüfung* **51** 405–11

[52]   Hiller J, Kasperl S, Hilpert U and Bartscher M 2007 Coordinate measuring with industrial X-ray computed tomography *Tech. Mess.* **74** 553–64

[53]   Lifton J J, Malcolm A A, Mcbride J W and Cross K J 2013 The application of voxel size correction in X-ray computed tomography for dimensional metrology *International NDT Conference & Exhibition* (Singapore) pp 19–20

[54]   Kiekens K, Welkenhuyzen F, Tan Y, Bleys P, Voet A, Kruth J-P and Dewulf W 2011 A test object with parallel grooves for calibration and accuracy assessment of industrial computed tomography (CT) metrology *Meas. Sci. Technol.* **22** 115502 http://dx.doi.org/10.1088/0957–0233/22/11/1

[55]   Carmignato S, Dreossi D, Mancini L, Marinello F, Tromba G and Savio E 2009 Testing of x-ray microtomography systems using a traceable geometrical standard *Meas. Sci. Technol.* **20** 084021 http://dx.doi.org/10.1088/0957–0233/20/8/08

[56]   Dewulf W, Kiekens K, Tan Y, Welkenhuyzen F and Kruth J-P 2013 Uncertainty determination and quantification for dimensional measurements with industrial computed tomography *CIRP Ann. - Manuf. Technol.* **62** 535–8

[57]   Vogeler F, Verheecke W, Voet A and Kruth J-P 2011 Positional stability of 2D X-ray images for computer tomography *International Symposium on Digital Industrial Radiology and Computed Tomography* (Berlin, Germany)

[58]   Uhlman N, Salamon M and Burtzlaff S 2008 Components and methods for highest resolution computed tomography *International Symposium on NDT in Aerospace* (Fürth, Germany) pp 3–9

[59]   Fröba T and Steffen J P 2011 The advancement of microfocus reflection tubes for industrial applications in measurement technology *50th Annual Conference of the British Institute of Non-Destructive Testing* (Telford, United Kingdom)

[60]   Weiss D, Deffner A, Kuhn C and Zeiss C 2010 Einfluß der quellbewegung auf reproduzierbarkeit und antastabweichung im röntgen-computertomographen *Conf. Ind. Comput. Tomogr.* 227–34

[61]   Weiß D, Lonardoni R, Deffner A and Kuhn C 2012 Geometric image distortion in flat-panel X-ray detectors and its influence on the accuracy of CT-based dimensional measurements *4th Conference on Industrial Computed Tomography (ICT)* (Wels, Austria) pp 175–81

[62]   Holt K M 2009 Geometric calibration of detectors with discrete irregularities for computed tomography *Proc. SPIE* **7258** 1–12

[63]   Welkenhuyzen F, Boeckmans B, Tan Y, Kiekens K and Dewulf W 2014 Investigation of the kinematic system of a 450 kV CT scanner and its influence on dimensional CT metrology applications *5th Conference on Industrial Computed Tomography (ICT)* (Wels, Austria) pp 217–25

[64]   Weitkamp T and Bleuet P 2004 Automatic geometrical calibration for X-ray microtomography based on Fourier and Radon analysis *Proc. SPIE Dev. X-Ray Tomogr. IV* **5535** 623–7

[65]   Sire P, Rizo P and Martin M 1993 X-ray cone beam CT system calibration *Proc. SPIE* **2009** 229–39

[66]   Sun Y, Hou Y, Zhao F and Hu J 2006 A calibration method for misaligned scanner geometry in cone-beam computed tomography *NDT E Int.* **39** 499–513

[67]   Sun Y, Hou Y and Hu J 2007 Reduction of artifacts induced by misaligned geometry in cone-beam CT *IEEE Trans. Biomed. Eng.* **54** 1461–71

[68]   Gullberg G T, Edgerton E R, Tsui M W and Crawford C R 1987 Estimation of geometrical parameters for fan beam tomography *Phys. Med. Biol.* **32** 1581–94

[69]   Gullberg G T, Tsui B M W, Crawford C R, Ballard J G and Hagius J T 1990 Estimation of geometrical parameters and collimator evaluation for cone beam tomography *Med. Phys.* **17** 264–72

[70]   Noo F, Clackdoyle R, Mennessier C, White T A and Roney T J 2000 Analytic method based on identification of ellipse parameters for scanner calibration in cone- beam tomography *Phys. Med. Biol.* **45** 3489–508 http://dx.doi.org/10.1088/0031–9155/45/1

[71]   Bequé D, Nuyts J, Bormans G, Suetens P and Dupont P 2003 Characterization of pinhole SPECT acquisition geometry *IEEE Trans. Med. Imaging* **22** 599–612

[72]   Bequé D, Nuyts J, Suetens P and Bormans G 2005 Optimization of geometrical calibration in pinhole SPECT *IEEE Trans. Med. Imaging* **24** 180–90

[73]   Von Smekal L, Kachelrieß M, Stepina E and Kalender W A 2004 Geometric misalignment and calibration in cone-beam tomography *Med. Phys.* **31** 3242–66

[74]   Yang K, Kwan A L C, Miller D F and Boone J M 2006 A geometric calibration for cone-beam CT systems *Med. Phys.* **33** 1695–706

[75]   Johnston S M, Johnson G A and Badea C T 2008 Geometric calibration for a dual tube/detector micro-CT system *Med. Phys.* **35** 1820–9

[76]   Xu J and Tsui B M W 2012 A graphical method for determining the in-plane rotation angle in geometric calibration of circular cone-beam CT systems *IEEE Trans. Med. Imaging* **31** 825–33

[77]   Xu J and Tsui B M W 2013 An analytical geometric calibration method for circular cone-beam geometry *IEEE Trans. Med. Imaging* **32** 1731–44

[78]   Taubin G 1991 Estimation of planar curves, surfaces, and nonplanar space curves defined by implicit equations with applications to edge and range image segmentation *IEEE Trans. Pattern Anal. Mach. Intell.* **13** 1115–38

[79]   Bequé D, Harrison D D, Basu S K and Fitzgerald P F 2007 Geometric model, control & calibration of universal benchtop CT system *IEEE Nucl. Sci. Symp. Conf. Rec.* **4** 2980–4

[80]   Rougée A, Picard C, Ponchut C and Trousset Y 1993 Geometrical calibration of X-ray imaging chains for three-dimensional reconstruction *Comput. Med. Imaging Graph.* **17** 295–300

[81]   Rougée A, Picard C, Trousset Y and Ponchut C 1993 Geometrical calibration for 3D X-ray imaging *SPIE Image Capture, Formatting, Disp.* **1897** 161–9

[82]   Bequé D, Vanhove C, Andreyev A, Nuyts J and Defrise M 2004 Correction for imperfect camera motion and resolution recovery in pinhole SPECT *IEEE Nucl. Sci. Symp. Conf. Rec.* **4** 2507–10

[83]   Defrise M, Vanhove C and Nuyts J 2008 Perturbative refinement of the geometric calibration in pinhole SPECT *IEEE Trans. Med. Imaging* **27** 204–14

[84]   Cho Y, Moseley D J, Siewerdsen J H and Jaffray D A 2005 Accurate technique for complete geometric calibration of cone-beam computed tomography systems *Med. Phys.* **32** 968–83

[85]   Ford J C, Zheng D and Williamson J F 2011 Estimation of CT cone-beam geometry using a novel method insensitive to phantom fabrication inaccuracy: Implications for isocenter localization accuracy *Med. Phys.* **38** 2829–40

[86]   Mennessier C and Clackdoyle R 2005 A Simple Analytic Method for Cone Beam Calibration *IEEE Nucl. Sci. Symp. Conf. Rec.* **5** 2743–6

[87]   Mennessier C and Clackdoyle R 2008 Automated geometric calibration and reconstruction in circular cone-beam tomography *IEEE Nucl. Sci. Symp. Conf. Rec.* 5081–5

[88]   Mennessier C, Clackdoyle R and Noo F 2009 Direct determination of geometric alignment parameters for cone-beam scanners *Phys. Med. Biol.* **54** 1633–60

[89]   Clackdoyle R and Mennessier C 2011 Cone-beam calibration using small balls: Centroids or ellipse centers? *IEEE Nucl. Sci. Symp. Conf. Rec.* 2763–7

[90]   Desbat L, Clackdoyle R, Grezes-besset L, Mennessier C and Bricault I 2006 Cone-beam imaging of delta functions *IEEE Nucl. Sci. Symp. Conf. Rec.* **2** 2859–63

[91]   Clackdoyle R and Mennessier C 2011 Centers and centroids of the cone-beam projection of a ball *Phys. Med. Biol.* **56** 7371–91